DEVELOPMENTAL NEUROSCIENCE

Lrrn-mediated retinal ganglion cell targeting drives visual circuit assembly for brightness and contrast detection

Elena Putti[1], Giulia Faini[1], Julie Thanh-Mai Dang[1], Jay H. Savaliya[2], Fanny Eggeler[1], Karine Duroure[1], Juliette Vougny[1], Gonzalo Ortiz-Álvarez[3], Cristina Pujades[3], Armin Bahl[2,4], Jeff W. Lichtman[2], Florian Engert[2], Jonathan Boulanger-Weill[1,2], Filippo Del Bene[1]*†, Shahad Albadri[1]*†

Brightness and contrast are fundamental features of vision, crucial for object detection, environmental navigation, and feeding. Here, we identify a brightness- and contrast-processing circuit in the zebrafish visual system and uncover the role of leucine-rich repeat neuronal (Lrrn) cell adhesion molecules (CAMs) in regulating its assembly. We show that deep-projecting retinal ganglion cells serve as the first synaptic relay to the brain, requiring Lrrn2 and Lrrn3a for precise axonal targeting within the optic tectum. Using a new reporter line, we achieved high-resolution mapping of this previously undercharacterized vertebrate visual circuit. Genetic disruption of Lrrn CAMs leads to disorganization of the circuit and impairments in brightness and contrast sensitivity, resulting in deficits in visually guided behavior. Additionally, ultrastructural circuit reconstruction and functional imaging analysis identified both its synaptic partners and revealed its critical role in luminance processing. These studies define a core visual processing pathway and establish Lrrn CAMs as essential molecular drivers of its assembly.

INTRODUCTION

Alterations in the formation of precise neuronal circuits profoundly affect nervous system function and subsequent behaviors, such as navigation and feeding that rely on brightness and contrast perception and integration (*1*–*4*). Yet, the developmental and molecular mechanisms governing their assembly are only partially understood. While diverse regulatory mechanisms—including transcription factors (*5*–*7*), axon guidance cues (*8*–*10*), and neuronal activity (*11*)—contribute to circuit formation, synaptic partner recognition is essential for neurons to establish precise connections (*12*–*16*). This final step in connectivity strongly relies on cell adhesion molecules (CAMs) (*14*, *17*–*20*).

The larval zebrafish has been extensively used as an optically accessible and genetically tractable vertebrate model for dissecting visual system circuits that underlie key aspects of perception, such as brightness and contrast (*21*–*23*). Retina ganglion cells (RGCs) axons project from the zebrafish retina to the optic tectum (OT), serving as the first relay of visual information to the brain. Within the OT, they establish synapses in 10 distinct laminae of the superficial neuropile (*24*, *25*). Each RGC projects exclusively to a single lamina, without innervating others, reflecting a high degree of specificity in this system. Among these, the stratum album centrale/stratum periventriculare (SAC/SPV) lamina, the deepest layer of the OT, has remained poorly characterized due to imaging and genetic targeting limitations (*26*, *27*). Using a novel RGC transgenic reporter enriched in this lamina [*Tg*(*gfi1ab:gal4*)], we identified leucine-rich repeat neuronal (Lrrn) CAMs as critical regulators of SAC/SPV-projecting RGC targeting.

Lrrn proteins belong to the leucine-rich repeat (LRR) family known for their roles, among others, in axon guidance (*8*, *9*), target selection (*5*, *28*, *29*), synapse formation (*30*, *31*), and their involvement in neurological disorders (*32*–*34*). In *Drosophila*, the Lrrn homolog Capricious (Caps) mediates photoreceptor targeting (*5*). In zebrafish, we show that four Lrrn family members are expressed in the retina, of which Lrrn2, Lrrn3a, and Lrrn3b are selectively expressed in RGCs. Using CRISPR-Cas9–mediated loss-of-function approaches, we demonstrate that Lrrn2 and Lrrn3a CAMs are required for the targeting of presynaptic SAC/SPV-projecting RGCs with their target neurons both in cell-autonomous and nonautonomous manners. Furthermore, the genetically induced disruption of this circuit leads to severe impairments in brightness and contrast processing, directly linking molecular mechanisms of circuit formation to visual function and behavior. By assigning a novel role to SAC/SPV-projecting RGCs, mapping their synaptic targets through electron microscopy (EM) segmentation, and integrating genetic, anatomical, functional, and behavioral analyses, our study provides additional insights into the genetic control of visual circuit assembly.

RESULTS

Shedding light onto deep-projecting RGCs

Although deep-targeting RGCs were identified decades ago, they remain poorly characterized, in part, because available pan-RGC transgenic lines do not efficiently label them (*35*). In addition, precise characterization of tectal laminae remains challenging due to the dense and overlapping projections of RGCs (*26*, *27*). To target specific subsets of these neurons, we sought to leverage the transcription factor growth factor–independent 1ab, *gfi1ab*, which is selectively expressed in a subset of RGCs (Fig. 1A) (*36*). Based on this specificity, we generated a novel transgenic reporter line, *Tg*(*gfi1ab:gal4*) (see Materials and Methods). The resulting line, when crossed with

[1]Sorbonne Université, INSERM, CNRS, Institut de la Vision, Paris 75012, France. [2]Department of Molecular and Cellular Biology, Faculty of Arts and Sciences, Harvard University, Cambridge, MA 02138, USA. [3]Department of Experimental and Health Sciences, Universitat Pompeu Fabra, PRBB, Barcelona 08003, Spain. [4]Centre for the Advanced Study of Collective Behaviour, University of Konstanz, Konstanz 78464, Germany.
*Corresponding author. Email: filippo.del-bene@inserm.fr (F.D.B.); shahad.albadri@inserm.fr (S.A.)
†These authors contributed equally to this work.

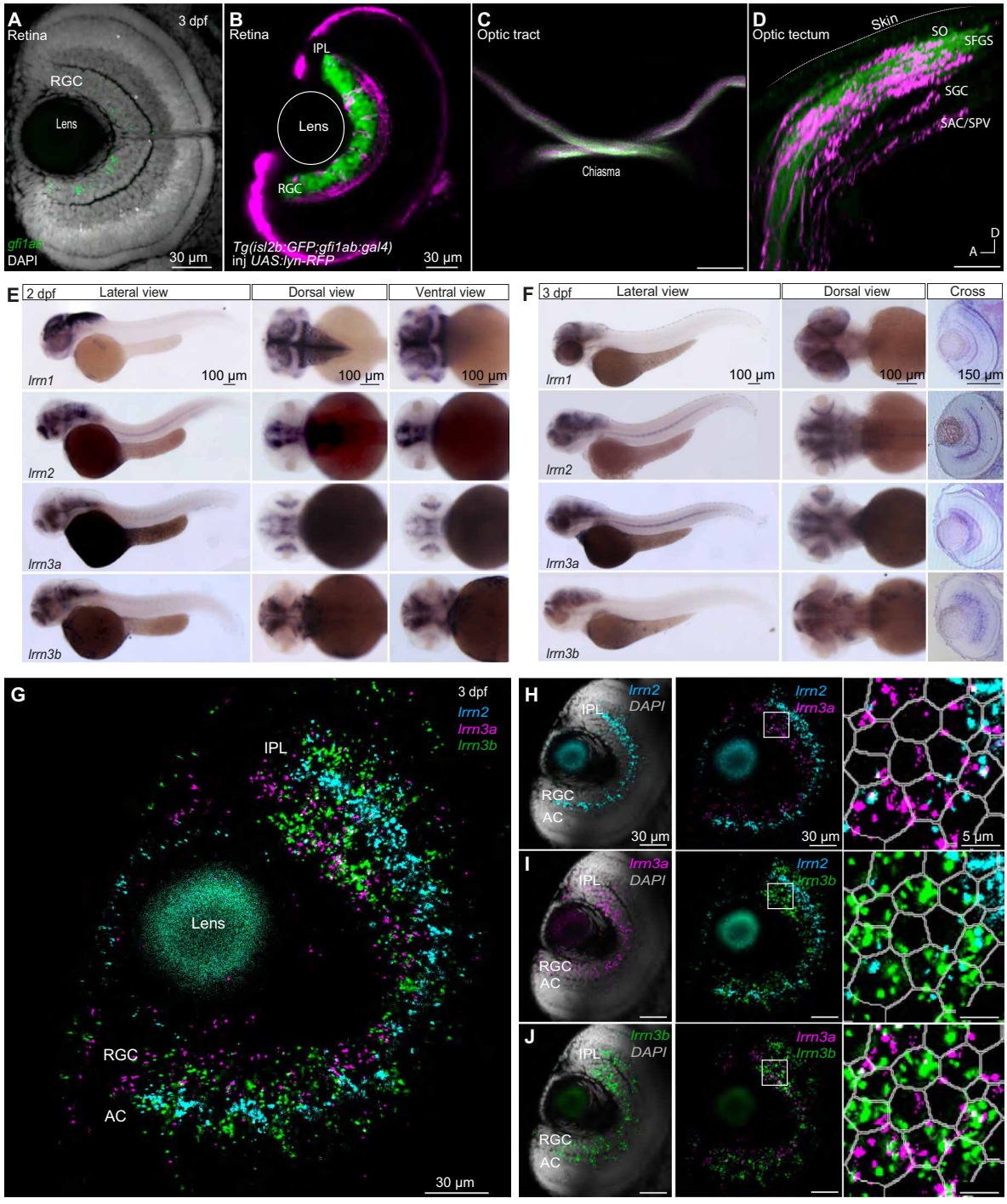

Fig. 1. *Gfi1ab* and *lrrns* are expressed in the developing RGCs of the zebrafish retina. (**A** to **D**) *Gfi1ab* sparse expression in RGCs at 3 days postfertilization (dpf). (A) Confocal stack of a 3-dpf zebrafish retina stained by whole-mount HCR in situ hybridization for *gfi1ab* (green) and DAPI (gray) highlighting cell nuclei. (B to D) Confocal images of 3-dpf *Tg*(*gfi1ab:gal4;isl2b:GFP*) embryos injected at the one-cell stage with a *10UAS:lynRFP* plasmid. (B) *Gfi1ab:gal4* expression (magenta) is sparse in RGCs compared to the pan-RGC marker Isl2b (green). (C) *Gfi1ab*-RGC axons crossing the chiasma at the midline. (D) *Gfi1ab*-RGC axons project within all sublaminae of the tectal neuropil. (**E**) Whole-mount in situ hybridization of all four *lrrn* isoforms at 2 dpf reveals broad expression in the forebrain, midbrain, and hindbrain. (**F**) Whole-mount in situ hybridization of all four *lrrn* isoforms at 3 dpf reveals their broad expression in the brain. Cross sections of the retina at 3 dpf show differential expression patterns within the neural retina of *lrrn1*, *lrrn2*, *lrrn3a*, and *lrrn3b*. (**G** to **J**) Confocal *Z*-stack images of a 3-dpf retina stained by multiplex HCR for *lrrn2* (cyan; hairpin fluorophore 594 nm), *lrrn3a* (magenta; hairpin fluorophore 633 nm), and *lrrn3b* (green; hairpin fluorophore 488 nm), showing their relative expression in the GCL and ACs. DAPI (gray) highlights retinal layers. Insets show magnified regions where Cellpose segmentation of DAPI borders was used to assess colocalization within RGCs. AC, amacrine cells; GCL, ganglion cell layer; IPL, inner plexiform layer; OT, optic tectum; RGC, retinal ganglion cells; SAC, stratum album centrale; SFGS, stratum fibrosum et griseum superficiale; SGC, stratum griseum centrale; SO, stratum opticum; SPV, stratum periventriculare.

Tg(*UAS:lynRFP*), faithfully reflected the endogenous *gfi1ab* sparse expression in RGCs (Fig. 1, A to D, and fig. S1, A and B), as well as in the pineal gland and ear hair cells, consistent with previous findings (*36*).

We then crossed *Tg*(*gfi1ab:gal;UAS:lynRFP*) fish with the pan-RGC marker *Tg*(*isl2b:GFP*) to analyze the projection profiles of *gfi1ab*-expressing RGCs in the retina (Fig. 1B) and OT (Fig. 1, C and D) of developing larvae. Although *gfi1ab* did not label a specific morpho-group of RGCs, it is expressed in a salt-and-pepper manner across different subpopulations (fig. S1, B to D). These Gfi1ab-RGC axons project to all OT layers, including stratum opticum (SO), stratum fibrosum et griseum superficiale (SFGS), and stratum griseum centrale (SGC), and particularly in the SAC/SPV layer (Fig. 1D). This unique enrichment of *gfi1ab* expression in SAC/SPV-projecting RGCs provides a novel tool for labeling deep-projecting axons in this tectal lamina that complements pan-RGC transgenic lines such as Tg(*isl2b:GFP*), where the strong fluorescence from superficial layers (SO/SFGS) makes challenging functionally imaging deeper projections (fig. S1, E and F).

In *Drosophila*, the ortholog of the zebrafish Gfi1ab transcription factor, Senseless, regulates the expression of the LRR CAM Caps, which plays a key role in photoreceptor targeting (*5*, *28*). We assessed the conservation of this pathway in vertebrates by performing an in silico search analysis (HomoloGene, National Center for Biotechnology Information) of Caps orthologs. We identified the Lrrn CAM protein family, comprising Lrrn1, Lrrn2, Lrrn3a, and Lrrn3b. Whole-mount in situ hybridization at 2 and 3 days postfertilization (dpf) revealed early and broad expression of all four paralogs in the fish's forebrain, midbrain, and hindbrain (Fig. 1, E and F). Retinal cross sections at 3 dpf showed *lrrn2*, *lrrn3a*, and *lrrn3b* expression in RGCs, with *lrrn2* and *lrrn3b* also present in the amacrine cell (AC) layer (Fig. 1F). Multiplex hybridization chain reaction (HCR) combined with confocal imaging showed that the expression of these three *lrrn* members partially overlap in the ganglion cell layer (GCL) (Fig. 1, G to J). Using Cellpose (*37*), we extracted the nuclear 4′,6-diamidino-2-phenylindole (DAPI)–derived signal, delineated the RGC membrane borders, and observed that the HCR signals colocalized within the same cells (Fig. 1, G to J). Quantitative HCR–based analyses revealed extensive combinatorial expression: Among *lrrn2*-expressing cells, ~60% also express *lrrn3a*, 65% express *lrrn3b*, and 47% coexpress both. Among *lrrn3a*-expressing cells, more than 50% express *lrrn2*, 65% express *lrrn3b*, and 43% express both. These results indicate that RGCs in the GCL display distinct but overlapping *lrrn* expression patterns.

Because the GCL contains both RGCs and displaced ACs, we next assessed the extent of displaced ACs expressing either *lrrn2* or *lrrn3a*. Using the *Tg*(*ptf1a:gal4;UAS:H2B-GFP*) line combined with multiplex HCR, we quantified the colocalization of *lrrn2* and *lrrn3a* with *ptf1a*-expressing cells, a pan-AC marker (fig. S1G). We found that ~30% of *lrrn2*-expressing cells and less than 12% of *lrrn3a*-expressing cells coexpress *ptf1a* in the GCL, indicating that most of *lrrn2*- and *lrrn3a*-expressing cells are RGCs and few displaced ACs.

Genetic loss of *gfi1ab* and *lrrn2/3a* leads to mistargeting defects in the deep-OT

To investigate the roles of Gfi1ab and Lrrn CAMs in vertebrates for RGC projections, we adopted a loss-of-function approach in zebrafish using CRISPR-Cas9–mediated knockout (KO) to either introduce early stop codons (*gfi1ab*$^{-/-}$) or disrupt the signal peptide and the LRR domains (*lrrn*$^{-/-}$) (see Materials and Methods) (fig. S2, A to C). All mutant lines generated were viable at homozygosity and showed no gross morphological defects.

We first assessed the impact of *gfi1ab* loss of function on *lrrn* CAMs expression levels in the larval visual system. To do so, we performed quantitative reverse transcription polymerase chain reaction (qRT-PCR) on the heads of *gfi1ab*$^{-/-}$ mutants and wild-type (WT) controls at 2 and 3 dpf. *Lrrn2* and *lrrn3a* mRNAs were significantly down-regulated in the absence of Gf1ab, particularly at 3 dpf (Fig. 2A and fig. S3A), while *lrrn3b* and *lrrn1* levels remained unchanged (fig. S3, B and C). For *lrrn2* and *lrrn3a*, we further confirmed this down-regulation specifically in RGCs by performing quantitative multiplex HCR on *gfi1ab*$^{-/-}$ mutants and WT controls at 3 dpf (fig. S3D). HCR experiments performed in 3-dpf *Tg*(*gfi1ab:gal4;UAS:lyn-GFP*) larvae showed notable colocalization of *lrrn2* (fig. S3E) and *lrrn3a* (fig. S3F) within *gfi1ab*-expressing cells. To more precisely assess the degree of colocalization between *gfi1ab* and the Lrrn family members, we performed multiplexed HCR to simultaneously label *gfi1ab*, *lrrn2*, and *lrrn3a* in the GCL (fig. S3, G and H). Leveraging the quantitative nature of multiplex HCR and the sparseness of the signals, we quantified transcript signals among *gfi1ab*-expressing RGCs. We found that ~52% of *gfi1ab*-RGCs express *lrrn2*, 73% express *lrrn3a*, and 38% coexpress both *lrrn2* and *lrrn3a*, while less than 14% express neither gene. These results indicate that *gfi1ab*-RGCs comprise distinct molecular subsets characterized by differential *lrrn* expressions. These observations further pinpoint a shared molecular pathway between Gfi1ab and Lrrn2/3a CAMs. In addition, qRT-PCR on the heads of *lrrn2* and *lrrn3a* mutant larvae, performed to assess expression changes in the other CAMs part of the *lrrn* subfamily, revealed a compensatory mechanism between both *lrrn2* and *lrrn3a* specifically. *Lrrn2* was up-regulated in *lrrn3a*$^{-/-}$ mutants (SM-3a) at 3 dpf (Fig. 2B), and, similarly, *lrrn3a* was up-regulated in *lrrn2*$^{-/-}$ mutants (SM-2) (Fig. 2B). In contrast, *lrrn3b* and *lrrn1* expression remained unchanged in both mutants (fig. S3, I and J).

Next, to evaluate the impact of the loss of Gfi1ab on *gfi1ab*-expressing RGC development, we imaged *Tg*(*gfi1ab:gal4;UAS:mRFP*); *gfi1ab*$^{-/-}$ larvae at 3 dpf when all RGCs should have projected their axons to the OT and reached their target layer. However, unlike WT control larvae, no fluorescence could be detected in the *gfi1ab*$^{-/-}$ mutant (fig. S3K). To investigate whether the absence of fluorescence was due to the loss of *gfi1ab*-expressing cell in its absence, we performed a terminal deoxynucleotidyl transferase–mediated deoxyuridine triphosphate nick end labeling (TUNEL) assay on *gfi1ab*$^{-/-}$ larvae, which revealed no increase in apoptosis compared to that in controls (fig. S3L). Furthermore, using DAPI staining and Cellpose, we measured no difference in the average cell number in *gfi1ab*$^{-/-}$ compared to that in WT central GCL at 3 dpf ($n = 7$ WT retinae/larvae and $n = 9$ *gfi1ab*$^{-/-}$ mutant retinae/larvae). These results suggest that *gfi1ab*-expressing cells are not lost. Rather, it suggests the presence of a self-regulatory mechanism of Gfi1ab on its own promoter that is disrupted in *gfi1ab*$^{-/-}$ mutants.

With *lrrn2* and *lrrn3a* down-regulated in *gfi1ab*$^{-/-}$ mutants, we evaluated the impact of their loss of functions as well as their combined depletion on *gfi1ab*-expressing RGC projections in the OT. We generated single- (SM) and double-mutant (DM) lines in the *Tg*(*gfi1ab:gal4;isl2b:GFP*) transgenic background and injected a *10UAS:lynRFP* plasmid into SM-2, SM-3a, and DM larvae at the one-cell stage, enabling single-cell analysis by mosaically labeling RGC membranes and axons. The *Tg*(*isl2b:GFP*) background served as a

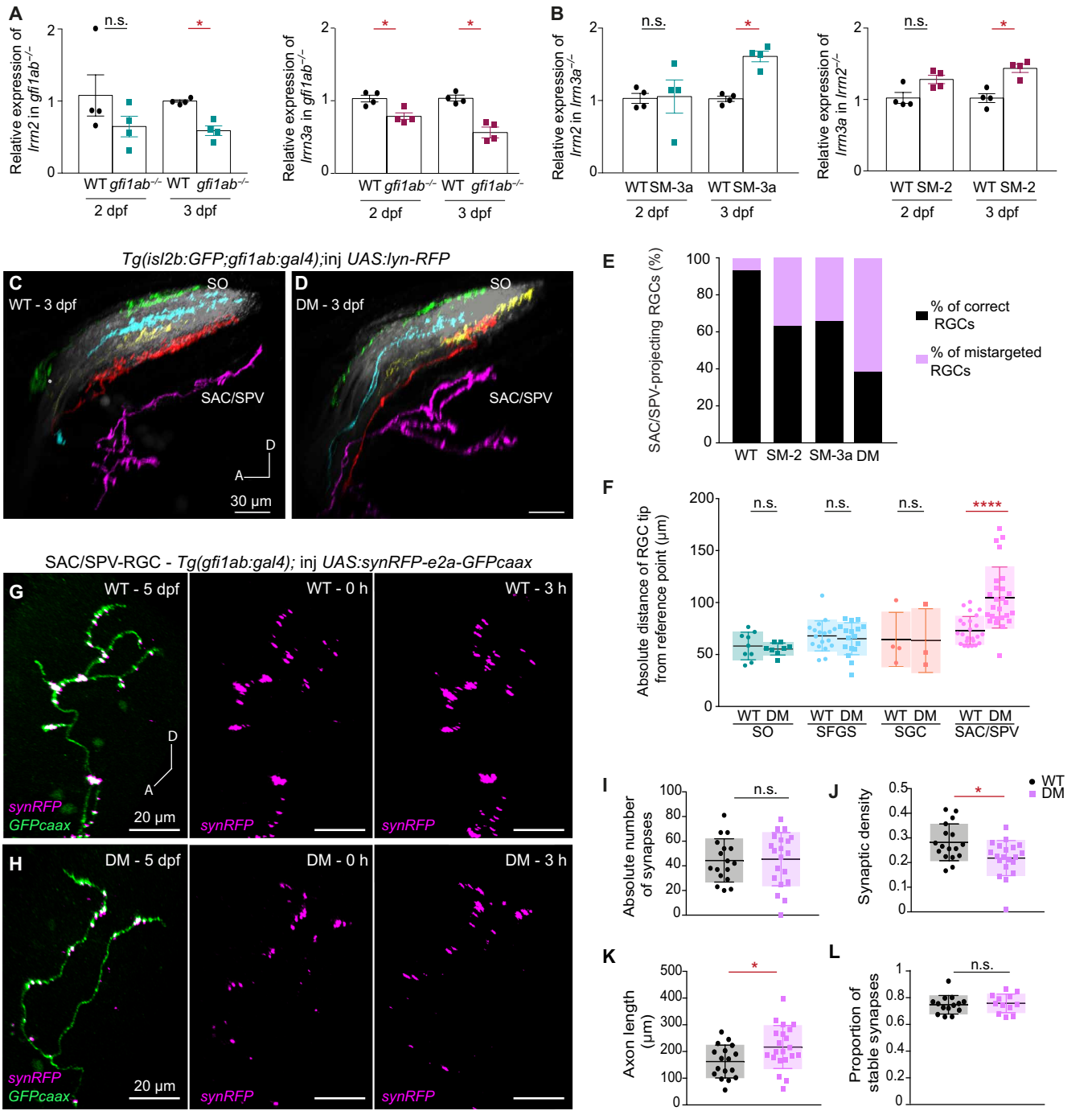

Fig. 2. *Gfi1ab* and *lrrns* KO impair RGC wiring assembly. (**A**) Quantitative reverse transcription polymerase chain reaction (qRT-PCR) analyses show significant down-regulation of *lrrn2* and *lrrn3a* at 2 dpf and at 3 dpf in *gfi1ab*$^{-/-}$. $P = 0.0286$ for all. (**B**) qRT-PCR analyses show significant up-regulation of *lrrn2* in SM-3a at 3 dpf ($P = 0.0286$) and *lrrn3a* in SM-2 at 3 dpf ($P = 0.0286$). (**C** and **D**) Gfi1ab RGCs target unique tectal laminae in WT, whereas DM shows mistargeting in the SAC/SPV layer. Confocal imaging of axonal projections of 3-dpf WT (C) and DM (D) *gfi1ab*-RGCs in the *Tg(gfi1ab:gal4;isl2b:GFP)* background injected with a *10UAS:lynRFP* construct for mosaic labeling of axonal projections. (**E**) Percentage of correctly targeted and mistargeted Gfi1ab-RGCs in WT, DM, and SM embryos. (**F**) Average absolute distances of RGC axonal tips from the skin for (C) and (D), showing a significant difference in the SAC/SPV layer of DM larvae compared to WT ($P < 0.0001$). (**G** and **H**) Confocal imaging of *gfi1ab*-expressing SAC/SPV-RGCs output synapses (magenta, synRFP) and axonal projections (green, GFPcaax) at 5 dpf in WT (G) and DM (H) at time point 0 and 3 hours later. h, hours. (**I**) Absolute number of synapses within SAC/SPV-projecting RGCs for (G) and (H), showing no difference between WT and DM larvae. (**J**) Synaptic density within SAC/SPV-projecting RGCs for (G) and (H), showing a significant difference between WT and DM larvae ($P = 0.0201$). (**K**) Average length of the SAC/SPV-projecting axons for (G) and (H), showing a significant difference between WT and DM larvae ($P = 0.0426$). (**L**) Proportion of stable synapses for (G) and (H), showing no difference between WT and DM larvae. Data are means ± SD. $P < 0.0001$. Statistical significance was determined by a Mann-Whitney *U* test: not significant (n.s.), $P > 0.05$; *$P < 0.05$; ****$P < 0.0001$. AF9, arborization field 9; A, anterior; D, dorsal.

reference to identify precise tectal laminae. While *lrrn* mutants did not show any obvious retinal or optic tract defects (fig. S3, M and N), SM-2, SM-3a, and DM larvae exhibited clear axonal mistargeting precisely in the SAC/SPV layer (Fig. 2, C to F, and fig. S4A). Compared to WT larvae, where red fluorescent protein (RFP)–positive RGCs projected to single and precise laminae of the OT, qualitative scoring revealed that more than 25% of SAC/SPV-projecting RGCs deviated from their normal target in the SM-2 and SM-3a larvae (Fig. 2E). DM larvae displayed even more severe defects than SM larvae, with >60% of deep-projecting RGCs exhibiting miswiring (Fig. 2E), suggesting an additive effect of *lrrn2* and *lrrn3a* losses. Tracing the different RGCs within the OT revealed no significant differences in RGCs projecting to the SO, SFGS, and SGC layers between DM larvae and WT controls (Fig. 2F). However, RGCs projecting to the SAC/SPV layer in DM larvae showed a significantly increased distance from the reference point on the skin compared to WT controls (Fig. 2F). These defects persisted at 5 dpf (fig. S4A), indicating that Lrrn2 and Lrrn3a are key CAM regulators of SAC/SPV targeting. To test whether these defects are due to an axon guidance impairment to the OT or a lamination/targeting phenotype, we also measured the distance from the skin at the axon deviation point before entering the SAC/SPV layer (fig. S4B). No difference was detected between WT and DMs (fig. S4B), excluding early guidance defects to enter the OT. Instead, DM axons overshot or deviated prematurely without terminating within the SAC/SPV layer. Similar SAC/SPV-related miswiring defects were also detected in the *gfi1ab*$^{-/-}$ larvae at 3 dpf injected with the *isl2b:gfp* plasmid at the one-cell stage (fig. S4C).

Last, we also investigated whether *lrrn3b*, also expressed in RGC, would induce defects in the axonal projections of Gfi1ab-RGCs when knocked out (KO). We thereby injected a *UAS:GFP* construct at one-cell stage to label *gfi1ab*-expressing RGCs in SM-2, SM-3a, and SM-3b larvae. Compared to those in SM-2 and SM-3a, no defects were observed in SM-3b larvae whose phenotype appeared to be reminiscent of those of WT control larvae (fig. S4, D to G).

To test whether synapse formation is impaired in DMs, we quantified the number of synapses formed by deep-projecting RGCs in the SAC/SPV layer. For this, we injected a *UAS:synRFP-E2A-GFPcaax* plasmid, which labels presynaptic puncta (*Synaptophysin-RFP*) together with the full axonal arbor (*GFPcaax*). The construct was injected at the one-cell stage into both WT and DM embryos in the *Tg*(*gfi1ab:gal4*) embryos, and RGCs were imaged at 5 dpf. To confirm that the analyzed puncta represent stable synapses, we imaged the same axons at an initial time point and again 3 hours later, following the approach of Meyer *et al.* (*38*) (Fig. 2, G to L). Loss of Lrrns did not alter the total number of stable presynaptic puncta per axon (Fig. 2L). However, DM SAC/SPV axons exhibited reduced synapse density as a consequence of their extended arbors. Specifically, the absolute number of puncta per axon was comparable between WT and DM (Fig. 2I), but the number of puncta normalized to axon length was significantly decreased in mutants (Fig. 2J), consistent with an increase in axonal length (Fig. 2K).

Last, to determine whether SAC/SPV-targeting RGCs directly express both *gfi1ab* and the CAMs *lrrn2* and *lrrn3a*, we performed multiplexed HCR experiments including *eomesa*, a specific marker of SAC/SPV-targeting RGCs in the retina (*27*). These experiments revealed strong coexpression of *eomesa* with *lrrn2*, *lrrn3a*, and *gfi1ab* (fig. S4H). Reanalysis of a published single-cell RNA-sequencing dataset of 2- and 3-dpf zebrafish retinae (*39*) confirmed that *eomesa*-positive cells also express *gfi1ab*, *lrrn2*, and *lrrn3a* (fig. S4I). Consistent with these findings, we simultaneously probed all four transcripts through multiplex HCR in situ hybridization and were able to identify RGCs coexpressing *eomesa*, *gfi1ab*, *lrrn2*, and *lrrn3a* (fig. S4J). Together, our results demonstrate that Lrrn2 and Lrrn3a function downstream of Gfi1ab in the vertebrate visual system, contributing to the accurate targeting of *gfi1ab*-expressing deep-targeting RGCs to the SAC/SPV layer of the OT.

Deep-targeting SAC/SPV RGCs molecular requirements for proper axonal projection

We then asked whether, at the cellular level, these CAMs are required within RGCs to achieve proper tectal lamination or act via non–cell-autonomous mechanisms. To address this, we performed cell transplantation assays at the blastula stage. First, we transplanted DM RGCs lacking Lrrn2 and Lrrn3a into a WT environment to determine whether defects persisted in a WT OT (Fig. 3A). Chimeric embryos were generated by transplanting donor cells from *10UAS:lynRFP*-injected WT or DM *Tg*(*gfi1ab:gal4*) embryos into WT *Tg*(*isl2b:GFP*) hosts of the same developmental stage (Fig. 3A). Confocal imaging of the resulting chimeric larvae at 3 dpf was performed to assess the axonal development of WT or DM *gfi1ab*-expressing RGCs devoid of Lrrn2 and Lrrn3a transplanted into WT. Our analysis revealed that mistargeting defects persisted when DM cells developed in a WT environment (Fig. 3, B and C), revealing a cell-autonomous requirement of Lrrn2 and Lrrn3a in RGC targeting (46%) (Fig. 3, D and E). Next, we assessed the contribution of the OT by transplanting WT RGCs (expressing *lrrn2* and *lrrn3a*) into a DM host (Fig. 3F). More than 44% of deep-projecting RGCs expressing both CAMs failed to reach their targets in the DM OT, differently from controls (Fig. 3, G to J). These results indicate that Lrrns are essential for proper axonal targeting both in the presynaptic retina and the postsynaptic partners in the OT.

Having established that Lrrns function in both pre- and postsynaptic compartments to regulate RGC targeting, we next sought to unravel the molecular mechanisms underlying their role in axon guidance. In *Drosophila*, Caps is thought to mediate targeting through homophilic binding interactions (*5*). To determine whether zebrafish Lrrns operate through similar or distinct mechanisms, we performed an in vitro protein aggregation assay to assess their binding properties. We asked whether, like Caps, Lrrn CAMs act through homophilic or heterophilic interaction or both. We performed an in vitro protein aggregation assay using human embryonic kidney (HEK) 293 cells transfected with *pCX:lrrn2-GFP* or *pCX:lrrn3a-RFP*, with *pCX:GFP* and *pCX:RFP* as controls (Fig. 3, K to R, and fig. S5, A to D). To evaluate homophilic interaction, aggregated cells expressing either Lrrn2–green fluorescent protein (GFP) or Lrrn3a-RFP showed an increased aggregation index compared to controls (Fig. 3, K to N and Q, and fig. S5, E to H). To assess whether both CAMs could interact through heterophilic binding, Lrrn2-GFP and Lrrn3a-RFP cells were coaggregated. We observed a higher number of aggregates coexpressing both fluorophores (Fig. 3, O, P, and R, and fig. S5, I to K). Together, these results indicate that Lrrn2 and Lrrn3a can bind through both homophilic and heterophilic interactions.

SAC/SPV-projecting RGCs and intertectal neurons converge onto OT projection neurons

Previous studies have shown that both neurons from the periventricular zone (PVZ) and nontectal neurons such as intertectal

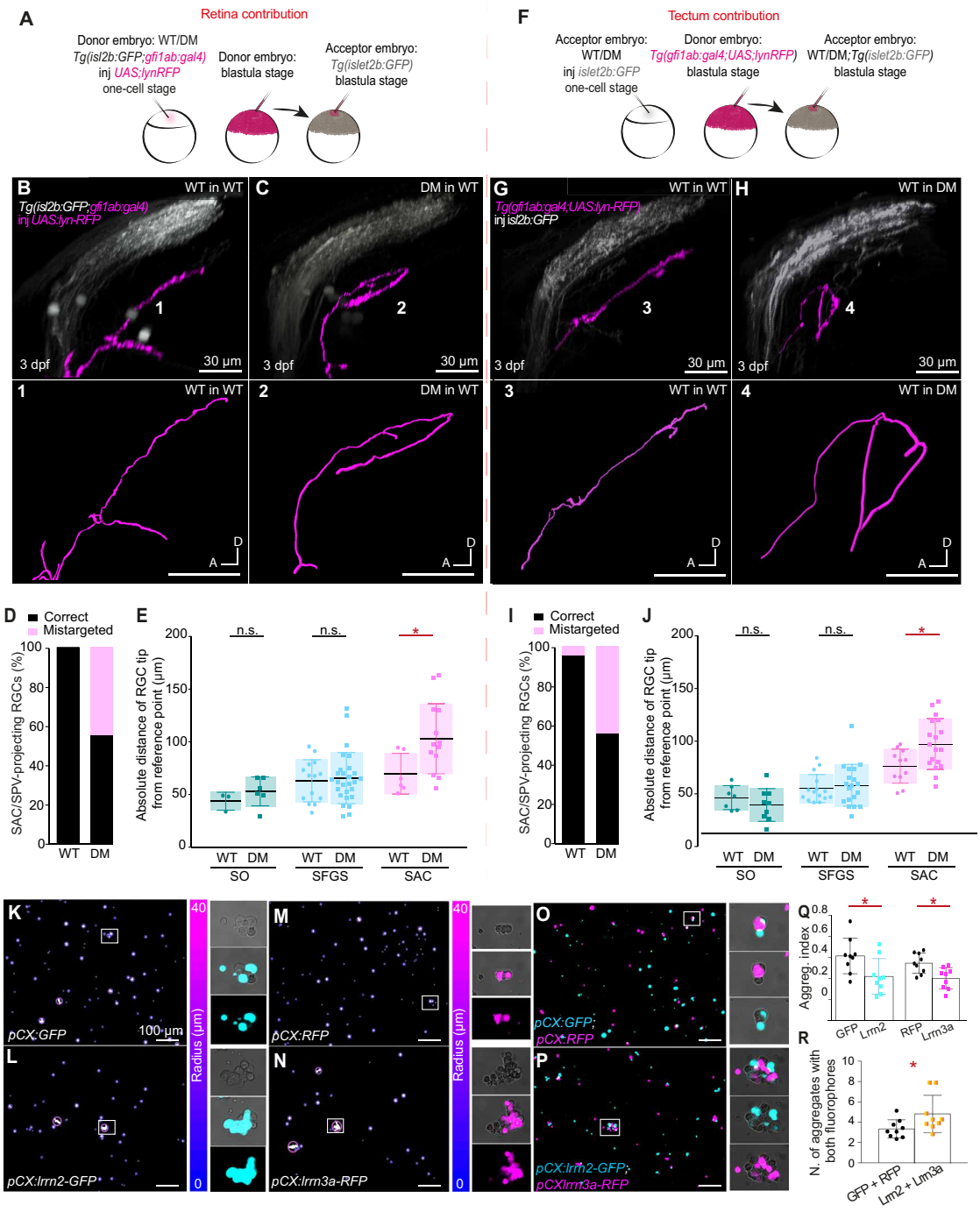

Fig. 3. Lrrn2/Lrrn3a are required in the retina and in the OT and act through homophilic and heterophilic interactions. (**A** and **F**) Transplantation workflows for assessing retina (A) and tectal (F) contributions of Lrrn2 and Lrrn3a for Gf1ab-RGCs projections. (**B** and **C**) Confocal images at 3 dpf of chimeras with WT (B) and DM (C) *gfi1ab*-RGCs transplanted into WT embryos, showing SAC/SPV-projections and misprojections (axons 1 and 2). Traced and magnified views of axons 1 and 2 are shown. (**D**) Percentage of correctly targeted and mistargeted SAC/SPV-RGCs in WT and DM transplanted into WT (WT = 6 and DM = 13 SAC/SPV-RGCs). (**E**) Axonal distances from the skin for (B) and (C) of the SAC/SPV-RGCs in DM and WT ($P = 0.0365$). (**G** and **H**) Confocal images showing WT *gfi1ab*-RGCs transplanted into WT (G) and DM embryos (H), highlighting SAC/SPV projections at 3 dpf (axons 3 and 4). Traced and magnified views of axons 3 and 4 are shown. (**I**) Percentage of correctly targeted and mistargeted SAC/SPV-RGCs in WT and DM transplanted into WT (WT = 12 and DM = 18 SAC/SPV-RGCs). (**J**) Axonal distances from the skin of the SAC/SPV-RGCs in DM and WT SAC/SPV-RGCs ($P = 0.0311$). (**K** to **N**) Aggregation assay of cells transfected with *pCX:GFP*. (K) or *pCX:RFP* (M) control plasmids. (L and N) Aggregation assay of HEK293 cells transfected with *pCX:lrrn2-GFP* (L) or *pCX:lrrn3a-RFP* (N), showing larger aggregates. (**O** and **P**) Coaggregation assays of cells transfected with *pCX:GFP* and *pCX:RFP* (O) or with *pCX:lrrn2-GFP* and *pCX:lrrn3a-RFP* (P), assessing heterophilic interactions. (**Q**) Aggregation index for control and Lrrn2/Lrrn3a overexpression conditions. (Lrrn2, $P = 0.04$; and Lrrn3a, $P = 0.0306$). (**R**) Number (N.) of aggregates coexpressing both GFP (cyan)/RFP (magenta) and Lrrn2 (cyan)/Lrrn3a (magenta). For (Q) and (R): Dots represent average values from nine independent experiments. Statistical analyses: nonparametric Mann-Whitney *U* test. Data represented as means ± SD. *$P < 0.05$. n.s., not significant.

commissural neurons (ITNs) can project to the deepest layers of the OT (*26*, *40*–*44*), but a comprehensive connectome remains unresolved. To address this, we performed an ultrastructural analysis using an EM dataset (*45*), which enabled us to reconstruct the detailed morphology and synaptic connectivity of SAC/SPV axons in the lower half of the OT (Fig. 4A and fig. S6, A and B). Across four traced RGCs, we detected axodendritic, axo-axonic, and axosomatic synapses with axodendritic contacts being most prevalent (Fig. 4B and fig. S6C). RGCs axodendritic inputs primarily targeted nonstratified periventricular interneurons (nsPVINs) and projection neurons (nsPVPNs) with a strong bias toward excitatory neurons (Fig. 4, C and D, and fig. S6, D to F).

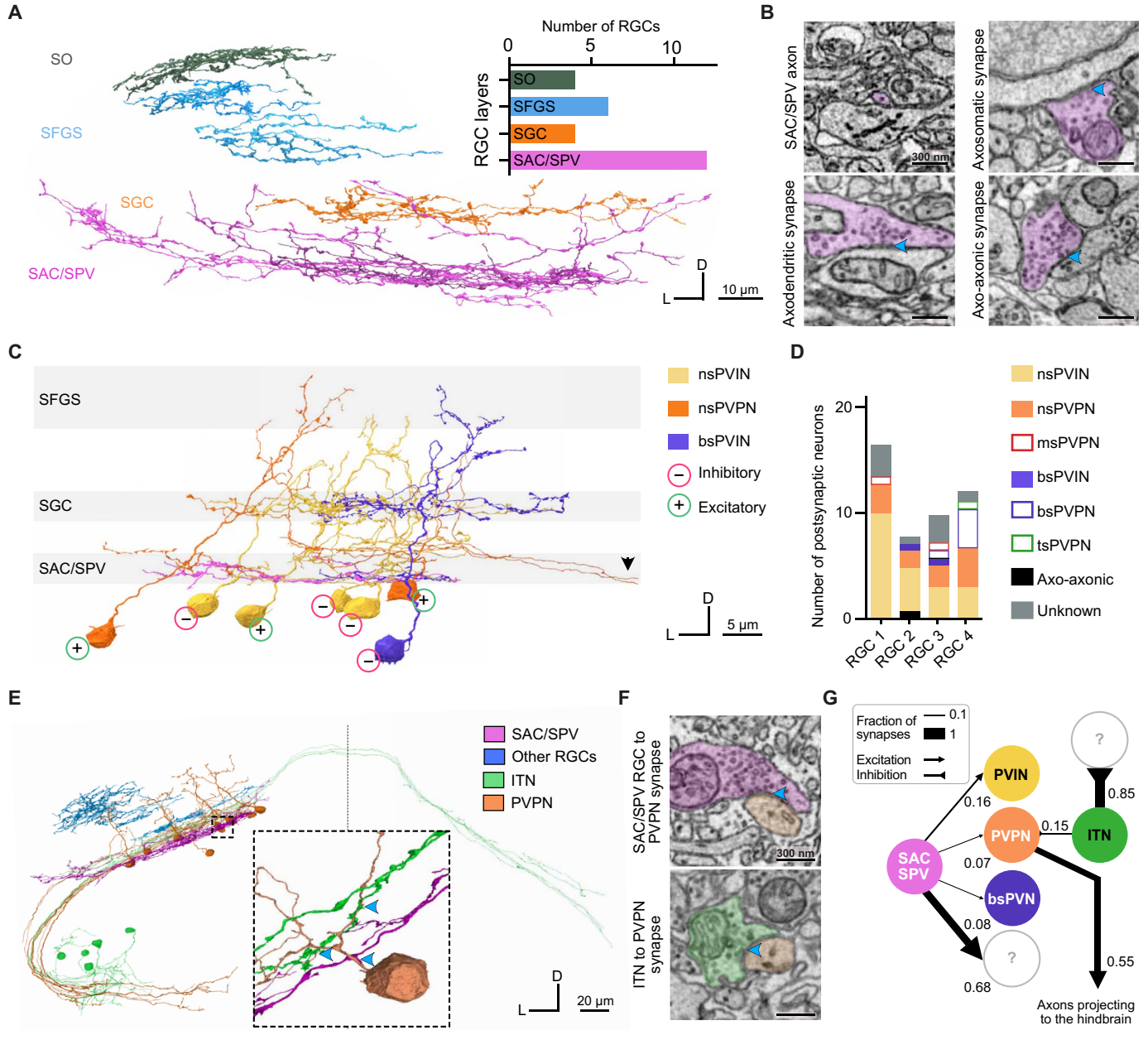

Fig. 4. Synaptic connectivity of SAC/SPV RGCs in the OT. (**A**) Coronal view of reconstructed RGCs spanning all layers of the left OT. The histogram shows the number of reconstructed RGCs per layer. (**B**) Example SAC/SPV axon forming multiple synapse types: axodendritic, axosomatic, and axo-axonic. (**C**) Sparse connectome of an example SAC/SPV axon (pink), displaying the most represented postsynaptic targets identified within the OT volume. The most superficial OT layers are not shown as none of the postsynaptic neurons innervated them. The arrow shows axons of PVPN neurons leaving the OT. (**D**) Bar plot showing the distribution of output PVN types for four SAC/SPV-RGCs. RGC no. 2 sparse connectome is shown in (C). (**E**) Reconstruction of ITNs, RGC axons, and PVPNs. The dashed vertical line marks the midline. The dashed inset highlights the anatomical connectivity of an SAC/SPV-projecting RGC and an ITN onto a PVPN neuron, with blue arrowheads indicating synapses; two examples are shown in (**F**). (**G**) Connectome of the main morphological types downstream of SAC/SPV RGCs. Connections representing less than 5% of total synapses are omitted. Question marks indicate either untraced partners or neurons not assigned to any morphological category. The dashed line marks the midline. PVIN, periventricular interneuron; PVPN, periventricular projection neuron; nsPVIN, nonstratified PVIN; nsPVPN, nonstratified PVPN; ms, mono stratified; bs, bistratified; ts, tristratified; s, stratified; D, dorsal; L, lateral.

ITNs extend axonal arbors into the deep OT layers, where they could receive synaptic inputs from deep projecting RGCs (*41*). Given this hypothesized connectivity in the deep OT where SAC/SPV axons also terminate, we asked whether ITNs form synapses with SAC/SPV-RGCs. To address this, we completely reconstructed three ITNs, identified by registering an image stack of a 6-dpf *Tg(*^{ITN}*Gal4;UAS:RFP;cry:GFP;HuC:H2B-GCaMP6s)* larva to the EM dataset (Materials and Methods and fig. S6G) (*45*). Although, we did not observe direct synaptic contacts between ITNs and SAC/SPV RGCs (fig. S6H), we identified nine PVPNs receiving convergent input from three ITNs and eight SAC/SPV RGCs (Fig. 4, E to G). A large fraction of these PVPNs projected to the hindbrain where they formed contacts with reticulospinal neurons (Fig. 4G and fig. S6I). Although the overall fraction of ITN and SAC/SPV synapses on PVPNs is likely underestimated in our sparse connectome reconstruction (Fig. 4G), these data support convergence onto PVPNs, mediated indirectly rather than by direct ITN/RGC axo-axonic connections.

Given that *lrrn2* and *lrrn3a* are expressed in the PVZ and that these nsPVINs and nsPVPNs are key targets of SAC/SPV axons, we wondered whether these periventricular neurons (PVNs) might be affected in our mutants. To address this question, we injected the *foxp2:gal4* plasmid and analyzed PVNs morphology in DM larvae, as previously performed (*46*). However, we did not find any difference in the proportion of stratified (sPVNs; which include mono-, bi-, and tri-stratified PVPN) versus nonstratified PVNs (nsPVNs; which include both nsPVPNs and nsPVINs) between WT and DM larvae (fig. S6, J and K), nor did we observe any clear mistargeting defect (fig. S6, J and K).

SAC/SPV-projecting RGCs are sensitive to luminance changes

Previous calcium imaging studies of the OT and pretectum have identified distinct functional groups within RGCs but had limited insights on the functional properties of the SAC/SPV layer (*26*, *27*, *47*). To address this knowledge gap, we used our *Tg(gfi1ab:gal4;UAS:GcaMP6s)* transgenic line. First, we used a battery of visual stimuli on the basis of those used in previous studies (*26*, *27*) and successfully subdivided the neuropil into five regions—SO, SFGS1, SFGS2, SFGS3, and SAC/SPV—according to their distance from the skin (Fig. 5, A and B). Functional responses in SO and SFGS regions were consistent with

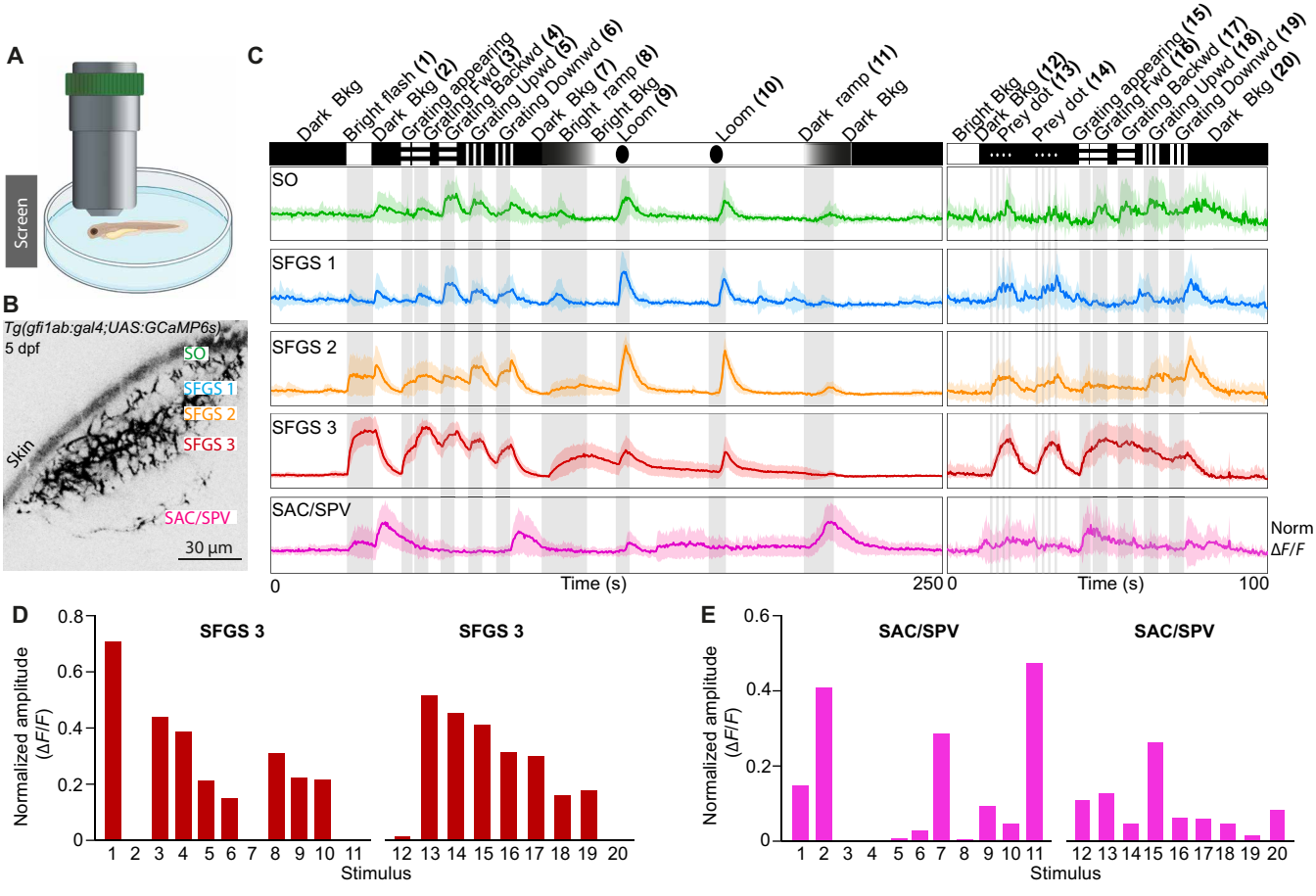

Fig. 5. Functional responses of SAC/SPV RGCs in the OT. (**A**) Illustration of the setup used for functional calcium imaging in in vivo 5- to 6-dpf larvae, with visual stimuli projected in front of the fish's eye. (**B**) Two-photon image of tectal lamination of a *Tg(gfi1ab:gal4;UAS:GcaMP6s)* 5-dpf embryo, with different regions within the volume discriminated. (**C**) Functional responses from distinct tectal regions shown in (B) to a series of visual stimuli (illustrated above the traces). Data are averaged across larvae ($n = 11$ for the first stimulus set and $n = 7$ for the second). Shaded areas represent SD. (**D**) Quantification of normalized response amplitudes (Δ*F*/*F*) for each stimulus in the SFGS 3 region, corresponding to the stimuli shown in (C). (**E**) Quantification of normalized response amplitudes (Δ*F*/*F*) for each stimulus in the SAC/SPV region, corresponding to the stimuli shown in (C). *F*, fluorescence intensity. Bkg, background; Fwd, forward; Upwd, upward; Downwd, downward.

prior findings (*27*), confirming the reliability of the stimulus set (Fig. 5, C and D, and fig. S7, A to D).

In contrast, in the SAC/SPV layer, we observed a robust activation to luminance changes, particularly when brightness decreased. This was most pronounced during dark and bright flashes (stimuli nos. 1 and 2 in Fig. 5C), as well as for the dark ramp stimulus (no. 11), and was also observed when the stimuli were turned off (e.g., nos. 7 and 20) (Fig. 5, C and E, and fig. S7A). To explore more specific responses, we presented prey-like stimuli and gratings independently of the standard stimulus battery. While the SAC/SPV layer showed some activation to prey-like dots (nos. 13 and 14), it did not generate a distinct fluorescence peak as seen in the more superficial layers. Notably, its response emerged slightly earlier and persisted longer. A similar prolonged response pattern was observed when gratings were reintroduced (nos. 16 to 19), an effect that had not been detected during the initial stimulus presentation, possibly because the preceding stimulus (appearance of a dark background, stimulus no. 2) elicited strong neuronal activation that masked subsequent responses (Fig. 5, C and E). Activation persisted even after the gratings were turned off, extending until the background transitioned to black. Together, these findings demonstrate that the SAC/SPV layer is highly sensitive to luminance changes, particularly to brightness decreases, but does not encode direction or orientation.

Similarly, we presented to 6-dpf DM larvae the same battery of visual stimuli and performed calcium imaging in the SAC/SPV layer of the OT. We found that *gfi1ab*-expressing RGC axons in DMs responded to the same stimuli as previously tested in WT larvae (fig. S7, E and F). This indicates that visual processing within the retina and the basic response properties of these RGCs are intact in DMs.

Altered SAC/SPV projections lead to impairments in brightness and contrast detection

The pronounced laminar defects observed in DM larvae raised the question of whether these structural abnormalities also led to visual impairments, especially given their distinct functional responses to dimming stimuli (Fig. 5C). To assess this, we first ruled out general motor impairments by tracking freely swimming 6-dpf WT and DM larvae for several minutes, finding no significant differences (fig. S8A).

To evaluate visual deficits, we initially examined the hunting behavior in 6-dpf larvae, as done in (*41*), in which the ablation of ITN cell bodies produces behavioral deficits in capture strikes. Initially, a prey-consumption assay was conducted to compare the overall hunting efficiency between DM and WT larvae. The assay revealed a significant reduction in the number of rotifers consumed by the DM larvae during the 4 hours of monitoring compared to WT controls (Fig. 6B), indicating a defect in prey capture. Similar deficits were observed for SM-2, SM-3a, and *gfi1ab*$^{-/-}$ larvae, revealing the involvement of this molecular pathway in the correct development of the neuronal circuits associated with this behavior (Fig. 6C and fig. S8B).

The hunting sequence comprises multiple stages from initiation to the capture of the prey, as previously described in other studies (Fig. 6A) (*41*, *48*, *49*). To further investigate the defects observed in the hunting sequence of DM larvae (Fig. 6B), we recorded 12-min videos where single larvae in presence of rotifers performed several hunting sequences (movies S1 and S2). Both WT and DM larvae spent a similar percentage of time foraging (fig. S8C) and hunting with converged eyes (Fig. 6D). Furthermore, there were no significant differences in the initiation of the hunting sequence (Fig. 6E), tracking (fig. S8C), target fixation (Fig. 6F), or any other steps leading up to predation (fig. S8C). However, DM larvae showed a significant impairment in initiating capture swims when the prey was within the strike zone (Fig. 6G). Although the mutants were able to approach the prey and get close to it, they often failed to initiate the stereotypical capture swims required for successful predation, opting instead to abort the hunting sequence and abandon the prey.

Additionally, optomotor response (OMR) assays indicated that both WT and DM larvae swam similar distances toward bright black and white and high-contrast (100, 50, and 35%) bars (Fig. 6H and fig. S8E), with comparable speeds and initiation latencies (fig. S8D). In contrast, DM larvae swam significantly less toward low-contrast and dimmer bars (20 and 10%) compared to WT controls and at a lower speed, highlighting a specific deficit in responding to reduced brightness and/or visual contrast (Fig. 6I and fig. S8, D and E). Instead, reducing the size of the moving bars did not affect the OMR response of the DM larvae (Fig. 6J), indicating no defect in visual acuity. The same specific OMR defect was also observed in *gfi1ab*$^{-/-}$ mutants (Fig. 6, K to M, and fig. S9, A to F). These findings demonstrate that the Lrrn2 and Lrrn3a pathway downstream of Gfi1ab plays a critical role in specific visually guided behaviors, particularly those requiring the visual detection of brightness and contrast.

DISCUSSION

Our work established Lrrn2 and Lrrn3a as key CAMs regulated by Gfi1ab guiding RGC axons to the SAC/SPV layer of OT, a previously uncharacterized microcircuit that we find essential for brightness and contrast processing. Lrrn CAMs are evolutionarily conserved both in spatial distribution and functions across species, underscoring their fundamental role in visual system development. In zebrafish and mouse (*50*, *51*), Lrrns are expressed in the retina, and, in *Drosophila*, their homologs localize to photoreceptors (*5*, *28*), suggesting shared molecular pathways across vertebrate and invertebrate visual systems (*12*). Functionally, we showed that DM larvae for Lrrn2 and Lrrn3a exhibit highly specific defects in RGC targeting, following correct axonal entrance into the OT. While projections to superficial OT layers remain intact, SAC/SPV innervation is specifically disrupted. Moreover, our transplantation experiments reveal that, like Caps, Lrrns operate both cell-autonomously in RGCs and non–cell-autonomously from the OT, ensuring precise targeting/and or termination, yet RGCs remain capable of forming synapses. While these findings establish Lrrns as necessary for proper SAC/SPV circuit formation in both tissues, it is possible that their role likely extends beyond direct homophilic or heterophilic interactions, as previously suggested for Caps (*5*, *17*, *52*). Although CAM overexpression increases aggregation, Lrrns may require in vivo additional heterophilic factors to promote or stabilize membrane complexes. This interplay and unique combination of factors likely refines target specificity within microcircuits that express the same molecules (*17*). The partial colocalization of Lrrns in the retina, specifically Lrrn2, Lrrn3a, and Lrrn3b, suggests that these proteins may either act redundantly in different combinations or have specialized roles in guiding distinct subsets of RGCs to specific tectal layers. This combinatorial organization resembles the interplay between Caps and its paralog Tartan in *Drosophila*, both contributing to photoreceptor targeting with overlapping but distinct functions (*53*, *54*). The absence of detectable targeting defects in the SAC/SPV layer of *lrrn3b* mutants indicates that its role may be either redundant with other Lrrns or confined to distinct RGC subtypes.

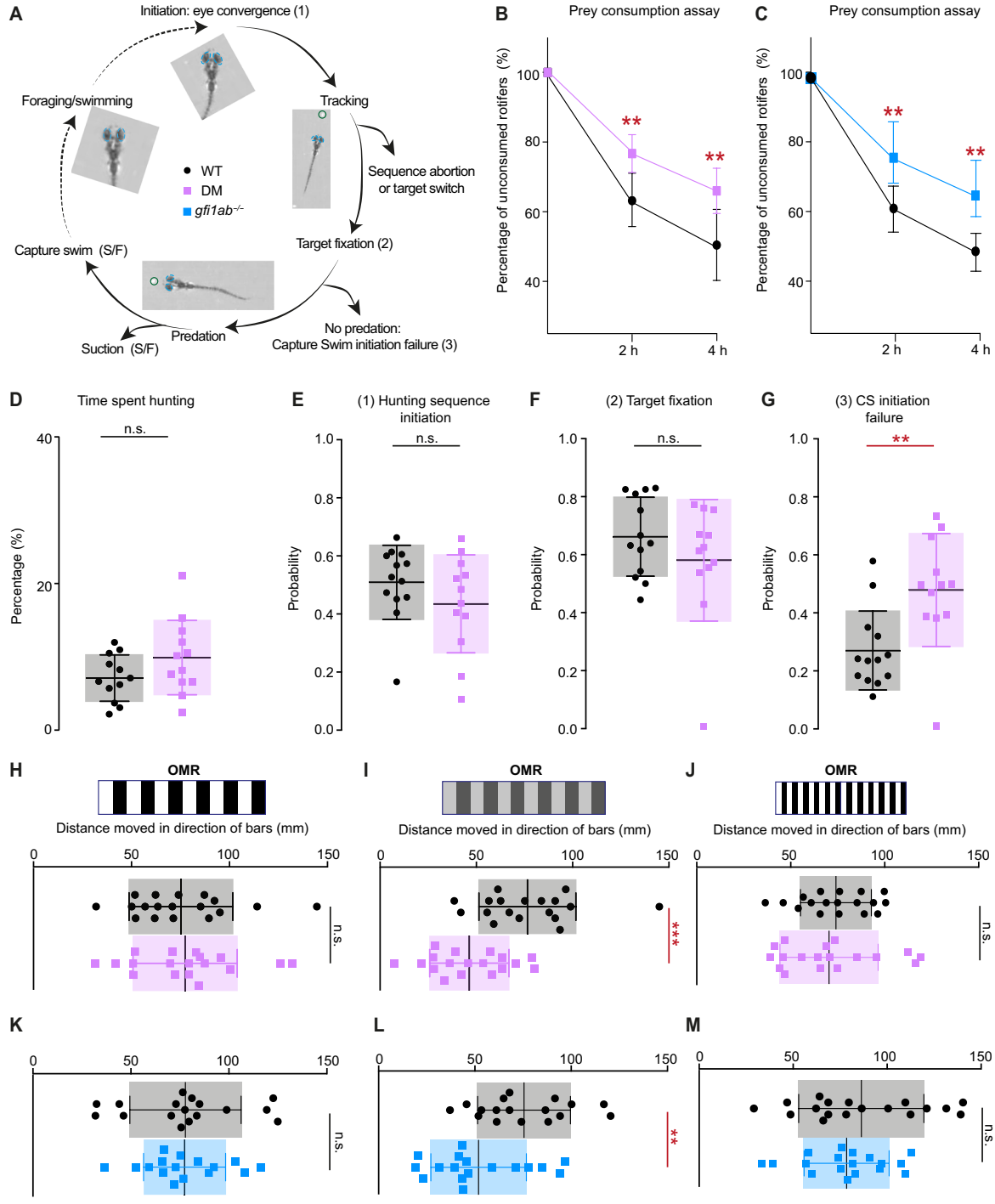

Fig. 6. Lrrn2, Lrrn3a, and Gfi1ab loss of functions lead to impairments in visually guided behaviors. (**A**) Representation of a complete 6-dpf larva hunting sequence. Converging eyes are circled in blue. (**B** and **C**) DM and *gfi1ab*$^{-/-}$ larvae consume significantly fewer rotifers than WT ($n = 10$ larvae per genotype; DM, $P = 0.0013$; and *gfi1ab*$^{-/-}$, $P = 0.0014$) after 2 and 4 hours. (**D**) Percentage of time spent hunting with converged eyes in 6-dpf WT and DM larvae. (**E** to **G**) Hunting sequence events in 6-dpf WT and DM larvae (total sequences: WT = 1084 and DM = 1249). (E) Hunting sequences initiation probability between WT and DM larvae. (F) Target fixation probability between WT and DM larvae. (G) Significant impairment of initiating capture swims in DM larvae and WT ($P = 0.0037$). (D to G) WT = 12 and DM = 12 larvae. (**H**) Distance swam by WT and DM larvae with 10-mm gratings at 100% contrast difference. (**I**) Distance swam by WT and DM larvae with 10-mm gratings at 20% contrast difference. DM larvae swim significantly less than WT ($P = 0.0006$). (**J**) Distance swam by WT and DM larvae with 4-mm gratings at 100% contrast difference. (**K**) Distance swam by WT and *gfi1ab*$^{-/-}$ larvae with 10-mm gratings at 100% contrast difference. (**L**) Distance swam by WT and *gfi1ab*$^{-/-}$ larvae with 10-mm gratings at 20% contrast difference. *Gfi1ab*$^{-/-}$ larvae show reduced swimming distance compared to WT ($P = 0.0095$). (H to L) WT = 18 and *gfi1ab*$^{-/-}$ or DM = 18 larvae. (**M**) Distance swam by WT and *gfi1ab*$^{-/-}$ larvae with 4-mm gratings at 100% contrast difference (WT = 17 and *gfi1ab*$^{-/-}$ = 18 larvae). Statistical analyses: nonparametric Mann-Whitney *U* test. Data represented as means ± SD. $^{**}P < 0.01$, $^{***}P < 0.001$. CS, capture strike; OMR, optomotor response. n.s., not significant.

Similarly to Sens controlling Caps in *Drosophila* (*5*, *28*), our analysis identifies Gfi1ab as a key regulator of *lrrn2* and *lrrn3a* in zebrafish, as they partially colocalize with *gfi1ab*-expressing RGCs and are down-regulated in the absence of Gfi1ab. When we examined *gfi1ab* mutants, we observed targeting defects within the SAC/SPV layer, providing direct evidence that its regulatory role influences RGC connectivity.

One of the main challenges in studying the SAC/SPV layer has been efficiently labeling this deep region of the tectal neuropile, as transgenic lines like *isl2b*, which mark *pan-RGCs*, do not adequately label the RGCs that project to this layer. Thus, prior functional imaging studies have struggled to directly capture the activity of the SAC/SPV layer, restricting our understanding of its role in higher-order visual processing. Previous efforts to address this gap have involved measuring functional responses from RGCs projecting to intermediate targets, such as arborization field 9 (*27*) or from PVN neurons that project within the deep neuropile (*26*). These studies have suggested a potential role for the SAC/SPV layer in responding to light intensity changes. In our study, the novel *Tg*(*gfi1ab:gal4;UAS:GcaMP6s*) transgenic line enables to directly capture RGC activity within the SAC/SPV lamina. We show that this layer is particularly responsive to luminance changes, with higher sensitivity to brightness decreases, especially during sudden or gradual shifts to dark backgrounds (stimuli OFF or dark ramp). Although these neurons respond more strongly to light decrements, they also activate upon presentation of light increment stimuli, suggesting that they do not conform strictly to ON or OFF selectivity. These results provide direct evidence that the SAC/SPV layer plays a specialized role in processing luminance shifts, which is essential for detecting dynamic visual cues in low-light environments.

The functional significance of the SAC/SPV layer is further supported by behavioral findings in DM mutants, which show a higher rate of prey-capture sequence failures, particularly during the critical transition to capture swims when prey is within the strike zone. Although these larvae can detect and approach prey, they fail to execute the precise capture swims necessary for successful hunting. Furthermore, while DM mutants respond robustly to OMR stimuli, even when the stimulus is presented at high spatial frequency, they struggle when contrast is reduced, indicating difficulty in perceiving decreased luminance variations.

Zebrafish have tetrachromatic vision, with cone photoreceptors sensitive to ultraviolet (UV, ~360 nm), short (blue, ~415 nm), medium (green, ~480 nm), and long (red, ~565 nm) wavelengths (*55*, *56*). While our behavioral setups did not include UV illumination, the spectral profile of the OMR setup has a broad illumination spectrum covering the short-, medium-, and long-wavelength ranges, similarly to the prey capture illumination setup, where we used live prey. These wavelengths are sufficient to activate multiple cone types and drive visually guided behaviors in both WT and our different zebrafish mutant larvae, as shown in prior work demonstrating robust prey capture and optomotor responses under broadband visible light conditions (*41*, *48*, *57*, *58*). Recent studies underscore the critical role of brightness and contrast as fundamental optical properties in prey detection, particularly for estimating target distance during the final strike decision (*3*). Our findings align with these observations, as DM larvae, which show defects in prey capture, also exhibit impaired responses to grating stimuli with reduced intensity and contrast. While their ability to detect prey at a distance remains intact, they may fail to accurately estimate its distance as it approaches or struggle to detect it altogether, leading to aborted strike attempts and inability to complete the hunting sequence. This suggests that the SAC/SPV layer, which is key in processing luminance cues, might be necessary for distance estimation. While Khan *et al.* (*3*) focused on the contribution of the UV, our findings conceptually align with this study in that reducing brightness or contrast (independently of spectral channels) diminishes cue strength perception against background. These features of the prey stimulus, whether fictive or live, are key at the capture strike initiation step to complete a successful hunting sequence. Future work could explore the relative contribution of each wavelength, including UV, and to which threshold. Because Lrrn molecules are also expressed in the OT and other brain regions, we sought to confirm whether the observed behavioral deficits stem specifically from retinal neurons. To address this, we tested *gfi1ab*$^{-/-}$ mutants, as Gfi1ab expression is restricted to RGCs in the retina and absent in the OT. These mutants exhibited the same prey-capture and OMR deficits as DM larvae, confirming that the observed phenotypes arise from RGC dysfunction rather than Lrrn expression in other brain regions. Furthermore, we did not observe clear defects in the morphology of downstream nsPVPNs and nsPVINs in DM larvae, although their nonstratified and variable dendritic morphologies and the lack of subpopulation markers make it difficult to rule out more subtle targeting differences. Nonetheless, we do not exclude that subtle miswirings within the OT, or impairments in other extra tectal visual circuits could also contribute to the observed behavioral deficits. At the same time, the identified role at the level of the retina alone is a critical first step to mediate this behavior as proven by our transplantation analysis and our behavioral assays on *gfi1ab*$^{-/-}$ mutants.

The behavioral deficits observed in DM larvae closely resemble those seen when the ITN cell bodies are ablated (*41*). In both DM mutants and ITN-ablated larvae, the capture strike step is selectively disrupted, hinting at a potential functional link between SAC/SPV-targeting RGCs and the ITNs. ITNs have been shown to be involved in the detection of the prey specifically at the moment when the prey enters the binocular strike zone, thereby enabling the initiation of capture swims through disinhibition of downstream circuits (*41*). Consistent with this, our connectomic analyses show that ITNs and SAC/SPV-targeting RGCs converge onto overlapping populations of PVPNs. This convergence provides a plausible circuit substrate through which SAC/SPV-RGCs inputs and ITN inputs could jointly regulate specific features of visually guided behaviors.

Overall, our study unravels a novel neural circuit from genetic and developmental components to functional output and anatomical connectivity, establishing the SAC/SPV layer as a key integrator of luminance processing and its downstream behavioral effects such as distance estimation. By bridging circuit development with visually guided behaviors, we provide insights into the molecular and structural mechanisms shaping deep tectal connectivity in a vertebrate brain.

MATERIALS AND METHODS

Fish lines and husbandry

Zebrafish (*Danio rerio*) were maintained under controlled conditions at a temperature of 28°C and subjected to a 14-hour light/10-hour dark cycle with sunset and sunrise. Embryos were collected and cultured in fish water supplemented with 0.003% 1-phenyl-2-thiourea to prevent pigmentation and 0.01% methylene blue (VWR, catalog no.

1.59270.0100) to inhibit fungal growth in the petri dish. The fish were housed within our institute's animal facility, constructed following local animal welfare standards. All animal procedures adhered to the ethical guidelines outlined by French and European Union regulations. Animal handling and experimental procedures were approved by the committee on ethics of animal experimentation of Sorbonne Université (APAFIS, no. 21323- 2019062416186982). Experimental procedures were conducted on larval zebrafish before the onset of sexual differentiation.

Zebrafish mutants and transgenic lines

The guide RNAs (gRNAs) used to generate the different CRISPR knock-in and KO lines are listed in table S1, and primers used for genotyping are listed in table S2. *Gfi1ab*$^{-/-}$ mutant line was generated using the CRISPR-Cas9 gene editing technology. A gRNA was used to target the first exon of the *gfi1ab* gene leading to a 4–base pair (bp) deletion, causing a frame shift in the open reading frame and a premature stop codon at the sixth amino acid, preventing any protein translation. For *lrrn2*$^{-/-}$ mutant line generation, two gRNAs were injected to target the first and single exon of the *lrrn2* gene leading to a large deletion of 308 bp, causing a disruption of the 5′ untranslated region (5′UTR) region, the deletion of the signal peptide of the gene, and a substantial portion of the LRR domain. It additionally introduced a frame shift and multiple premature stop codons, preventing any protein translation. For *lrrn3a*$^{-/-}$ mutant line generation, two gRNAs were injected to target the first and single exon of the *lrrn3a* gene leading to a large deletion of 302 bp, causing a disruption of the 5′UTR region, the deletion of the signal peptide of the gene. Like for *lrrn2*, the generated deletion triggered a nonsense-mediated decay as measured by qRT-PCR. For *lrrn3b*$^{-/-}$, three guides were injected to generate a full KO in the F0 generation (*59*), creating a 1000-bp cut and the deletion of most of the LRR domain, preventing any protein translation. PCR amplicons were deposited on 1 to 3% agarose (LifeTechnologies, catalog no. 16500500) gel for the identification of WT and mutants. For all the generated mutations, we also confirmed their effect using the SMARTprot software that modeled the protein translation outcome upon the induced deletion.

The *gfi1ab:gal4* bacterial artificial chromosome (BAC) construct was generated as follows: A BAC spanning the *gfi1ab* genomic locus (CH211-164G7, BACPAC Resources Center) was used to perform Tol2 transposon–mediated BAC transgenesis introducing *gal4* instead of the *gfi1ab* coding sequence by PCR-based homologous directed recombination and bacterial resistance selection. Transformation through electroporation of the *pRedET* plasmid was performed as described (*60*). For Tol2 transposon–mediated BAC transgenesis, the iTol2-amp cassette was amplified by PCR with the primer pair pTarBAC_HA1_iTol2_fw (5′-gcgtaagcggggcacatttcattacctctttctc-cgcacccgacatagatCCCTGCTCGAGCCGGGCCCAAGTG-3′) and pTarBAC_HA1_iTol2_rev (5′-gcggggcatgactattggcgcgccggatcgat-ccttaattaagtctactaATTATGATCCTCTAGATCAGCTC-3′), where the lower and upper cases indicate the *pTarBAC2.1* sequences for homologous recombination and the *iTol2-amp* annealing sequences, respectively. Subsequently, the amplified *iTol2-amp* cassette was introduced into the backbone (*pTarBAC2.1*) of the Gfi1ab-BAC. The PCR product (500 ng; 1 ml) was used for electroporation. 5′-gactgtccgattctcactaatgactggggacatatgaggcagaggaggacGCCAC-CATGAAGCTACTGTCTTCT ATCGAAC-3′ and 5′-ggctggtggtagct-gtgcgctttttgctcttcaccaagaaagacctaggCCGCGTGTAGGCTGGAGCT-GCTTC-3′ primers were used to amplify and insert the *gal4FF* cassette into the BAC (*61*). The lower and upper cases indicate the CH211-164G7 sequences for homologous recombination and the *pGal4FF-FRT-Kan-FRT* annealing sequences, respectively. The PCR product (500 ng; 1 ml) was used for electroporation in *Gfi1ab-iTol2-amp-BAC*–containing cells. The BAC DNA preparation was performed using the HiPure Midiprep kit (Invitrogen, catalog no. K2100), with modifications for BAC DNA isolation as described by the manufacturer. Tol2 transposase mRNA was prepared by in vitro transcription from Not I–*linearized pcs2-tol2* (*62*) using the T7 mMessage mMachine kit (Ambion, catalog no. Am1348). RNA was purified using the RNeasy purification kit (QIAGEN, catalog no. 74104), diluted to a final concentration of 100 ng/μl for injection. At least 50 injected fish were backcrossed to WT. Germline transmission was observed in the offspring from two of such crossings with identical patterns reminiscent of endogenous *gfi1ab* expression.

Along with the newly generated and validated *Tg*(*gfi1ab:gal4*) line, three other transgenic lines expressing *GFP* or *RFP* were used in this study: the previously published *Tg*(*isl2b:GFP*) (*63*) and the previously published *Tg*(*UAS:RFP;cry:GFP*) transgenic line (*64*). The *UAS:GCaMP6s* transgenic line was generated by injecting the *14UASubc:GCaMP6s* plasmid with *tol2* transposase mRNA at 25 ng/μl in one-cell stage zebrafish embryos. To generate the plasmid, we cloned GCaMP6s from plasmid 59530 (Addgene) and inserted it into the 14UASubc backbone, using the NEBuilder HiFi DNA Assembly Cloning Kit (New England Biolabs, catalog no. E5520S) following the manufacturer's instructions. The *Tg*(*ptf1a:gal4*) transgenic line was generated by injecting with *tol2* mRNA the *ptf1a:Gal4:polyA;cmcl2:EGFP* plasmid. The cloning of this plasmid was done using the Gateway LR Clonase II Enzyme mix (Thermo Fisher Scientific, 11791020), according to manufacturer's instructions, and using plasmids from K Kwan's Tol2kit (*65*). The entry clones used were a homemade p5E-*ptf1a* vector, a *pME-Gal4FF* vector (middle entry clone containing the Gal4FF sequence, gifted by Virginie Lecaudey, Goethe-Universität, Frankfurt, Germany) and a *p3E-polyA* vector (3′ entry clone including the SV40 late polyA signal). The *p5E-ptf1a* vector was produced via Gibson cloning (New England Biolabs, E5510S), following the manufacturer's instructions and the *ptf1a:DsRed2* plasmid (*66*) (gifted by M. Brand, TU Dresden, Germany) as amplification template for *ptf1a* promoter. As destination vector, we used the *pDestTol2CG2* vector, which comprises Tol2 transposition sequences and encodes a *cmlc2:EGFP* transgenesis marker that expresses EGFP in the fish' heart. The resulting *Tg*(*ptf1a:Gal4:polyA;cmcl2:EGFP*) reporter line was crossed with a *Tg*(*UAS:H2B-GFP*) line and the *Tg*(*ptf1a:Gal4:polyA;cmcl2:EGFP;UAS:H2B-GFP*) embryos were stained at 1 dpf by HCR in situ hybridization on endogenous *ptf1a* mRNA allowing the validation of this new reporter line. Significant colocalization between GFP protein signals and endogenous *ptf1a* mRNA signals could be detected in the hindbrain where it is first expressed at this developmental stage (fig. S1, G and H).

Molecular cloning

The p*UAS:lyn-GFP* plasmid was generated as previously described (*46*). The *pUAS:lynRFP* construct used in this study was previously cloned by Auer and Del Bene (2014) (*64*). The *pDest-Tol2-Isl2b:GFP:polyA* was obtained from Addgene (plasmid no. 105648). The *pCX:lrrn2-eGFP* and *pCX:lrrn3a-RFP* were generated by modifying the *pCX:eGFP* and *pCX:RFP* plasmids from Coralie Fassier. *lrrn2* and *lrrn3a* cDNA was obtained from 3-dpf larvae total RNA extraction. *Lrrn2* and *lrrn3a* cDNA were subsequently subcloned into the

pCX:eGFP or *pCX:RFP*, respectively, using the NEBuilder HiFi DNA Assembly Cloning Kit (New England Biolabs, E5520S) following the manufacturer's instructions. The *pfoxp2.a:Gal4FF* plasmid was obtained from Nikolau and Meyer (2015) (*9*). The *pUAS:synRFP-e2a-GFPcaax* plasmid was obtained from (*67*).

Microinjections

Fertilized eggs were collected in egg medium and aligned into prepared 2% agarose (LifeTechnologies, catalog no. 16500500) injection molds (agarose diluted in water) (Adaptive Science Tools, catalog no. TU-1). To inject, a pressure injector [PicoPump with pressure (WPI, catalog no. PV820), Manual Micromanipulator (WPI, catalog no. M3301R), and Injection Assembly parts kit (WPI, catalog no. MMP-KIT) with borosilicate glass capillaries (WPI catalog no. GBF100-50-10)] was used. The capillaries were previously filled with the following injection solutions and injected through the chorion into the cytoplasm of the single cell. The *10UAS:lynRFP* and *UAS:lynGFP* plasmid was injected at 10 ng/µl with or without 20 ng/µl of *tol2* mRNA, either for broad or sparse cellular labeling. The *isl2b:GFP* plasmid was injected at 25 ng/µl with *tol2* mRNA (20 ng/µl). The *foxp2:gal4FF* plasmid was injected at 15 ng/µl with *tol2* mRNA (10 ng/µl).

Whole-mount NBT/BCIP single in situ hybridizations

Total zebrafish cDNA ranging from stages 48 to 72 hours postfertilization (hpf) was amplified for probe synthesis. In vitro transcription of digoxigenin/fluorescent-labeled probes was carried out using an RNA Labeling Kit (DIG RNA Labeling Mix, catalog no. 11277073910; Fluorescein RNA Labeling Mix, catalog no. 11685619910, Roche) following the manufacturer's protocols. Zebrafish whole-mount in situ hybridizations were conducted as previously outlined. Subsequently, stained embryos were captured using a stereomicroscope (Leica, catalog no. MZ10F). Image processing and analysis were conducted using ImageJ software, with uniform adjustments made for color balance, brightness, and contrast.

Vibratome sections

Whole-mount embryos were washed a few times in 1× phosphate-buffered saline (PBS)/0.1% Tween 20 (PBS-Tw) solution after whole-mount nitro blue tetrazolium/5-bromo-4-chloro-3-indolyl-phosphate (NBT/BCIP) in situ hybridization (Roche, catalog no. 11681451001). The samples were embedded in gelatin (Sigma-Aldrich, catalog no. G1890)/albumin (Sigma-Aldrich, catalog no. A4503) with 4% of glutaraldehyde (Sigma-Aldrich, catalog no. 340855) and sectioned (20 mm) on a vibrating blade microtome (Leica, catalog no. VT1000 S). Sections were mounted in Fluoromount Aqueous Mounting Medium (Sigma-Aldrich, catalog no. F4680).

TUNEL assay

To detect apoptosis on whole-mount zebrafish larvae at 4, 5, and 7 dpf, the TUNEL assay was used, using the Apoptag Peroxidase In Situ Apoptosis Detection Kit (Millipore, catalog no. S7100). Larvae at 4, 5, and 7 dpf were fixed in 4% paraformaldehyde (PFA; Electron Microscopy Sciences, catalog no. EM-15710) diluted in PBS (Euromedex catalog no. EU1-9400-100) with 0.1% Tween 20 (Sigma-Aldrich, catalog no. 0777) for 2 hours at room temperature (RT) and then dehydrated and stored in methanol (MeOH; Thermo Fisher Scientific, catalog no. 15623710) at −20°C. Dehydrated larvae fixed at the proper developmental stages were rehydrated at RT using successive and decreasing dilutions of MeOH in 1X phosphate-buffered saline with Tween 20 (1X PBST). The samples were then washed in PBST. To allow the permeabilization of the samples and the penetration of the probe, the larvae were digested at RT with Proteinase K (10 µg/ml; Sigma-Aldrich, catalog no. 03115852001) diluted in PBST for 45 or 60 min, according to their developmental stage. Proteinase K digestion was stopped by incubating the samples in 4% PFA (in PBST) for 20 min or more at RT. Several washes were carried out using PBST before incubating the larvae in 100% ethanol (VWR, catalog no. 84857-360)/100% acetic acid (VWR, catalog no. 20104.298), mixed 2:1, at −20°C for 15 min. Several washes were then performed in PBST at RT. The larvae were then equilibrated in the Equilibration Buffer provided by the kit at RT for 15 min. The samples were then transferred to terminal transferase enzyme solution mixed with the Reaction Buffer 1:2 (both in the Apoptag kit) and 3% Triton X-100 (Euromedex, catalog no. 2000-C)/PBS for 1 hour on ice and then for 1 hour at 37°C. Stop Solution (1%; from the kit) was used to stop the transferase reaction for 5 min at RT and then for 45 min at 37°C. Several washes were then carried out in PBST. The larvae were then incubated for at least 1 hour in 10% Blocking Solution (Roche, catalog no. 11096176001) to saturate the nonspecific binding sites before adding antibodies anti–DIG-Fab fragments conjugated to alkaline phosphatase (Roche, catalog no. 11093274910) diluted 1:5000 in 2× Blocking Solution. The samples were incubated in this solution overnight at 4°C. A series of PBST washes were performed the next day before incubating the samples in the Staining Buffer [5 M NaCl, 1 M $MgCl_2$, 1 M tris-HCl (pH 9.5), 100% Tween 20, H_2O] twice for 10 min at RT. The color reaction was then carried out by incubating the larvae with NBT/BCIP (Roche, catalog no. 11681451001) diluted 1:500 in the Staining Buffer in total darkness for as long as necessary. To stop the reaction, the larvae were washed several times with PBST and then fixed overnight at 4°C in 4% PFA in PBST. The samples were then analyzed on ZEISS SteREO Discovery.V20 microscope after an overnight incubation at 4°C in 87% glycerol (VWR, catalog no. 24388.295) diluted in water.

Cryo-sectioning

Zebrafish larvae at of 3 or 5 dpf were fixed in 4% paraformaldehyde in 1× PBS (pH 7.4) for 2 hours at RT and, thereafter, cryo-protected overnight in a 30% sucrose (VWR, catalog no. 27480.294)/0.02% sodium azide (Sigma-Aldrich, catalog no. S2002)/PBS solution. Embryos were transferred to plastic molds and embedded in O.C.T. Compound (Euromedex, catalog no. 62550-12) after removal of the sucrose. Blocks were then frozen at −80°C on dry ice. The 14-µm sections were mounted on Superfrost Plus slides (Thermo Fisher Scientific, catalog no. 10149870).

Immunohistochemistry

For anti-GFP immunohistochemistry, no antigen retrieval was performed, and 1:500 dilution of chicken primary anti-GFP antibody (GeneTex, catalog no. GTX13970, RRID:AB_371416) and Alexa Fluor 488 secondary antibody goat anti-chicken immunoglobulin G (1:1000, LifeTechnologies, catalog no. A-11041, RRID:AB_2534098) were used. Immunohistochemistry experiments were performed as follows: Cryo-sections were washed three times in 1 × 3 PBS/0.1% Tween 20 (PBS-Tw) solution. Consecutively, slides were incubated 1 hour at RT in 10% blocking solution (Roche) followed by overnight incubation at 4°C in 1% blocking solution (10% blocking solution in 1× PBS-Tw) in which primary antibodies were diluted. Sections

were then washed five times using 1 × 3 PBS-Tw solution and incubated at RT for 1 to 2 hours in 1% blocking solution in which primary antibodies were diluted. Slides were then washed several times in 1× PBS-Tw solution, counterstained with DAPI (LifeTechnologies, catalog no. D3571), and diluted in 1× PBS-Tw solution for 10 min. The DAPI solution was then washed out several times in 1× PBS-Tw solution. Slides were then mounted using an 80% glycerol solution before imaging.

Multiplex HCR in situ hybridization

All HCR probes and buffers (version 3) were purchased from Molecular Instruments. Larvae (48 to 72 hpf) underwent fixation in 4% paraformaldehyde in PBS (pH 7.4) for 2 hours at RT, followed by multiple rinses with PBS to halt the fixation process. Subsequently, larvae were subjected to dehydration through a series of MeOH washes and then stored at −20°C. The HCR procedure was carried out according to the manufacturer's instructions. HCR fluorescent samples were then imaged using a 40× inverted immersion objective [numerical aperture (NA), 1], with *Z*-volumes captured at a resolution of 1.5 μm, using an Olympus FV3000 confocal microscope. Image processing and analysis were conducted using ImageJ and Cellpose software. The first was used to extract maximum projections of two to four stacks while the latter to segment DAPI signal to retrieve nuclei's outline membrane borders. These membrane outlines were used to better identify cells coexpressing RNAs of interest.

HCR puncta were extracted using ImageJ particle analysis plugin, excluding particles smaller than 0.02 pixel^2 to remove background noise, and assigned to DAPI-labeled nuclei or *ptf1a*-expressing cells using custom MATLAB scripts. Membrane borders were first extracted using Cellpose, and punctae were considered colocalizing if they fell within the membrane borders. Coexpression categories were calculated for each cell. Analyses were performed across multiple independent experiments.

Transplantation

Mutant and WT chimeric embryos were obtained by blastomere transplantations at the 1000-cell stage as previously described (*68*). Donor RGCs were derived from *Tg*(*lrrn2*$^{-/-}$;*lrrn3a*$^{-/-}$;*gfi1ab:gal4*) mutant or *Tg*(*lrrn2*$^{+/+}$;*lrrn3*$^{+/+}$;*gfi1ab:gal4*) WT embryos, previously injected at one-cell stage with *UAS;lyntagRFP* and transferred into either *Tg*(*isl2b:GFP*) or *Tg*(*lrrn2*$^{-/-}$;*lrrn3a*$^{-/-}$;*gfi1ab:gal4;isl2b:GFP*) acceptor embryos of the same stage.

Aggregation assay

The aggregation assay was performed as described (*69*). To evaluate homophilic interaction, HEK293 cells (RRID:CVCL_0045) were independently transfected with *pCX:eGFP*, *pCX:mRFP*, *pCX:lrrn2-eGFP*, and *pCX:lrrn3a-mRFP*. Images of three random areas per well were acquired for each sample and averaged to yield one value, using a Leica DM6000 Epifluorescent Microscope with a 10× objective. The aggregation assay was performed in nine independent experiments.

At the start of the assay (time point 0), cells were resuspended into single-cell suspensions. A portion of transfected cells was transferred to six-well plates and used as controls, while the remaining cells were subjected to aggregation. Small spontaneous aggregates may form immediately after resuspension due to the nature of the used cell type as reported in (*69*).

Fluorescent signals from single cells or aggregates were detected and counted semiautomatically using a custom-made MATLAB code. This code detected and highlighted structures on the basis of a pixel intensity threshold. The detected structures were circled with colors that varied on the basis of the radius of each structure. Various images were also manually evaluated to validate the code. Images of the three random areas per well were averaged together. The aggregation index was calculated as the number of particles detected in the aggregated wells divided by the number of particles in the control wells at time point 0, which is normalized to 1.

To evaluate heterophilic interaction, cells were independently transfected with *pCX:eGFP*, *pCX:mRFP*, *pCX:lrrn2-eGFP*, and *pCX:lrrn3a-mRFP*. Before starting the aggregation protocol, *pCX:eGFP*-transfected cells were mixed with *pCX:mRFP* cells, and *pCX:lrrn2-eGFP*–transfected cells were mixed with *pCX:lrrn3a-mRFP* cells and imaged as controls. Image acquisition was performed as before, and homophilic interaction was tested as well. To evaluate possible interaction between Lrrn2 and Lrrn3a, we manually counted the aggregates expressing both red and green fluorophores and normalized the total number of coexpressing aggregates after aggregation to the number of coexpressing aggregates before aggregation at time point 0.

mRNA extraction and cDNA preparation and qRT-PCR

Total mRNA extraction was conducted from dissected heads of 2- and 3-dpf zebrafish larvae using TRIzol reagent (LifeTechnologies, catalog no. 15596018) and TURBO DNA-free reagents (Ambion, AM1907). The mRNA was derived from a mix of the heads of 50 larvae of the same genotype. The concentration of mRNA was determined using the NanoDrop 2000 (Thermo Fisher Scientific). For reverse transcription, 1 μg of mRNA was retro-transcribed using random primers, and the SuperScript III First-Strand Synthesis system (LifeTechnologies, catalog no. 18080051). SYBR Green PCR Master Mix (Ambion, catalog no. 4368702) was used for qRT-PCR on QuantStudio 6 PCR System instrument (Thermo Fisher Scientific) according to the manufacturer's instructions. *Ef1a* and *rpl13a* were used as reference genes, as previously documented. All assays were conducted in technical triplicates and replicated in four independent biological experiments. Data are means ± SD, and 50 heads per condition were used.

Mean values from triplicate experiments were determined using the delta cycle threshold (CT) quantification method, with *P* values calculated using a Mann-Whitney nonparametric test. The primers used for qRT-PCRs are in table S3.

Comparison between *Tg*(*gfi1ab*) and *Tg*(*isl2b*) lines

Fluorescence intensity was quantified using ImageJ [National Institutes of Health (NIH)] to compare visualization of the SAC/SPV layer in *Tg*(*gfi1ab*) and *Tg*(*isl2b*) transgenic fish lines. For each image, obtained through confocal microscopy, pixel intensity was measured in both the SFGS and SAC/SPV layers. To normalize fluorescence across images and reduce image-to-image errors, a fluorescence index was calculated by dividing the mean intensity of SAC/SPV by the mean intensity of SFGS within each image. This analysis was performed in both transgenic lines to assess differences in imaging quality.

Confocal imaging

Mutant and WT control RGC axons, as well as PVNs, were acquired from 3- and 5-dpf live larvae, using a 40× Wplan Apochromat objective [numerical aperture (NA), 1; working distance (WD), 2.5 mm], with *Z*-volumes captured at a step size of 1.5 μm, using an Olympus FV3000 laser scanning confocal microscope. Image acquisition was

conducted at a resolution of 1024 × 1024 pixels, with a scan rate of 4 μs/pixel. The same imaging approach was used for the transplantation experiments. HCR imaging was conducted on 3-dpf fixed larvae, using the same parameters and settings, except for the scan rate at 8 μs/pixel.

Single-RGC analysis

To analyze signal from the *Tg*(*gfi1ab:gal4*) transgenic line, the three-dimensional (3D) reconstructions of the *Z*-volumes of RGCs axons were obtained using the Oxford Imaris Suite software 10.0. 3D images were rotated to visualize the synaptic laminae. Skin autofluorescence and the signal from the retina were removed manually. To isolate single-RGC axons, we used the surface tool with semiautomatic selection and then applied the surface to mask the RGC when its projections were clearly distinguishable from other axons. We then used the filament tracing tool to properly trace the RGC and calculate its absolute distance from a reference point positioned manually. Such reference point was consistently positioned on the skin and 3D oriented using the signal from the *Tg*(*isl2b:GFP*) background. When traced RGCs presented several arborizations, we calculated independently the absolute distance from the tip of each arborization to the reference point, which were then averaged to obtain a unique value for each RGC. Depending on the distance from the skin, each RGC was identified as SO, SFGS, or deep-projecting RGC. Statistical analysis was conducted separately for RGCs projecting to different layers. A similar analysis was performed to quantify the distance from the reference point to the entry point of the OT. The percentage of correct and mistargeted deep-projecting RGCs was also assessed phenotypically and compared between mutants and WT controls.

To analyze the projections of RGCs labeled by the *Tg*(*isl2b:GFP*) plasmid, we used syGlass, a virtual reality software, in combination with an Oculus Quest (Meta) headset. This approach was essential, as conventional methods using Imaris alone were insufficient for the detailed tracking of individual axon projections. In syGlass, we used the region of interest (ROI) tool to manually track and segment the axons in 3D and generate masks. The final segmented images were saved as TIFF files, which were compatible with Imaris 10.0, allowing us to visualize and manipulate multiple channels/masks. The datasets were organized to maintain the same dimensionality as the original data, enabling precise visualization of the axon projections with distinct pseudocolor assignments.

Single-PVN analysis

The 3D reconstructions of the Z-volumes of PVNs were obtained using the Oxford Imaris Suite software. 3D images were rotated to visualize the neuron's morphology. Skin autofluorescence and the signal from the retina were removed manually. The quantification of stratified vs nonstratified neurons was performed as in (*46*).

Synapse quantification in SAC/SPV-projecting RGCs

To quantify output synapses of deep-projecting RGCs in the SAC/SPV layer, we used a *UAS:synRFP-E2A-GFP-CAAX* plasmid, which labels presynaptic puncta (Synaptophysin-RFP) and the full axonal arbor (GFP-CAAX). The construct was injected at the one-cell stage into WT and DM embryos, and individual RGCs were imaged at 5 dpf. To confirm that the detected puncta represented stable synapses, axons were imaged twice, separated by 3 hours, following the approach of Meyer *et al.* (*38*). Presynaptic puncta were manually counted, axonal length was measured using ImageJ, and 3D visualization and validation of puncta distribution were performed with Oxford Imaris Suite. Synapse density was calculated as the number of RFP-labeled puncta per axon length.

Behavioral tests

Free swimming

Free swimming behavioral acquisitions, fish tracking, tail segmentation, and analysis were performed as previously described (*70*, *71*). In total, 12 larvae were tested for each genotype with the acquisition lasting for 20 to 30 min.

Optomotor response

To assess the OMR in our fish, we used the Stytra software platform (*72*). The fish were tracked using Stytra, which provided precise tracking data, and the videos were recorded at 100 Hz. The same camera and illumination setup as in the free-swimming experiment was used. Visual stimuli were projected below the 60-mm petri dish via a cold mirror. The visual stimuli consisted of sinusoidal gratings of 4- and 10-mm spatial frequency and a speed of 10 mm/s. Contrast levels were varied to probe sensitivity, using high-contrast gratings (100% contrast) and progressively lower contrasts of 50, 35, 20, and 10%. These contrast changes jointly modulate the brightness of the applied stimulus. The stimulus consisted of six repetitions of 20 s of either left-ward or right-ward movements, alternating after 20-s pauses. The larvae were left to adapt to a light illuminated background before stimulus presentation for over 15 min. Subsequently, we used a custom-made Python code to extract detailed parameters from the tracking data, including trajectories, speed, tail beat frequencies, distances, and latency. To minimize the effect of directional bias, we averaged the total distances moved during leftward and rightward bar presentations.

Prey capture assay

Prey consumption assays were conducted at 6 dpf and performed as previously described (*41*).

Prey capture sequence

To assess the outcomes of individual hunting sequences, 12-min videos capturing hunting larvae were recorded at a rate of 100 Hz. Darkfield illumination was achieved by using a custom-made LED-ring (wavelength, 850 nm) positioned around the dish, facilitating the detection of rotifers. Hunting sequences were identified on the basis of observable eye vergences and categorized according to their outcomes. The spectra of the different light sources used in the behavioral assays are shown in fig. S10 (400 to 750 nm, in 1-nm increments).

Zebrafish larva used for two-photon imaging and the EM connectomic atlas

The triple transgenic *Tg*(*elavl3:H2B-GCaMP7f*$^{+/+}$;*gad1b:dsRed*$^{+/-}$;*kdrl:mCherryCAAX*$^{+/-}$) larva used in this study was obtained by crossing adult transgenic *Tg*(*elavl3:H2B-GCaMP7f; gad1b:DsRed*) and *Tg*(*elavl3:H2B-GCaMP7f; flk1:mCherryCAAX*) lines in nacre background, *mitfa*$^{-/-}$ (*73*), yielding high GCaMP7 fluorescence. All experiments were approved by the Harvard University standing committee on the use of animals in research and training. At 7 dpf, the larva was embedded in a drop of agarose (UltraPure Low Melting Point Agarose; Invitrogen, catalog no. 16520050), at ~35°C at the center of a petri dish (9 cm in diameter; Dutscher, catalog no. 633180). After the agarose was solidified, the dish was filled with fish facility water and transferred into the measurement chamber of a custom-built two-photon microscope, operated by custom-written

Python 3.7–based software (PyZebra2P). We used a femtosecond-pulsed laser (MaiTai Ti:Sapphire, Spectra Physics) equipped with a set of *x*/*y*-galvanometers (Cambridge Technology), a 20× infrared-optimized objective (XLUMPLFLN, Olympus) to scan over the brain and two photomultipliers (green and red) amplified by two current preamplifiers (SR570, Stanford) to collect fluorophores emissions.

Sample preparation for EM imaging

The following protocol was specifically modified from (*74*) to enhance the extracellular space preservation, which improves synapses detection and permits single-cell resolution imaging using x-ray tomography. Unless noted, all steps were performed at RT. Immediately after the two-photon stack acquisition, the larva still anesthetized and embedded in agarose, we replaced the water by a dissection solution [64 mM NaCl, 2.9 mM KCl, 10 mM Hepes, 10 mM glucose, 164 mM sucrose, 1.2 mM $MgCl_2$, and 2.1 mM $CaCl_2$ (pH 7.5)] supplemented with 0.02% tricaine (Sigma-Aldrich, catalog no. E10521) (*75*). We then cut small slits in the agarose to expose the eyes and performed bilateral enucleations to enhance ultrastructural preservation (extracellular space) and heavy metal staining. We used a custom-made hook that was carefully inserted behind the eyes to prevent brain damage. The larva was immediately transferred to a fixation solution at 4°C (2.5% glutaraldehyde and 0.1 M cacodylate buffer supplemented with 4.0% mannitol at pH 7.4). Cacodylate buffer: 0.3 M sodium cacodylate and 6 mM $CaCl_2$ (pH 7.4). To improve the fixation, the tissue was rapidly microwaved (catalog no. 36700, Ted Pella, equipped with power controller, steady-temperature water recirculator and cold spot) in the fixative solution (this step lasted <5 min after initial transfer into fixative). The microwaving sequence was performed: at power level 1 (100 W) for 1 min ON, 1 min OFF, and 1 min ON then to power level 3 (300 W) and fixed for 20 s ON, 20 s OFF, and 20 s ON, three times in a row. Fixation was then continued overnight at 4°C in the same solution. The following day, the sample was then washed again in 0.5× cacodylate buffer (three exchanges, 30 min each before osmication; 2% OsO_4 in 0.5× cacodylate buffer, 90 min). After a quick wash (<1 min) in 0.5× cacodylate buffer, the sample was reduced in 2.5% potassium ferrocyanide in 0.5× cacodylate buffer for 90 min, then washed with filtered H_2O (three exchanges, 30 min each), and then incubated with 1% (w/v) thiocarbohydrazide (TCH) in filtered H_2O (and filtered with a 0.22-μm syringe filter before use) for 45 min to enhance staining (*76*). Due to poor dissolution of TCH in water, the solution was heated at 60°C for ~90 min with occasional shaking before filtering and then placed at RT for 5 min before the incubation step. The sample was then washed with filtered H_2O (three exchanges, 30 min each) before the second osmication (2% OsO_4 in filtered H_2O, 90 min) and then washed again (three exchanges, 30 min each). Then, en bloc staining was performed overnight using 1% uranyl acetate in filtered water at 4°C. The solution was sonicated for 90 min and filtered with a 0.22-μm syringe filter before use. Steps involving uranyl acetate were performed in the dark. The following day, samples were then washed with filtered H_2O (three exchanges, 30 min each). Next, the samples were dehydrated in serial dilutions of ethanol (25, 50, 75, 90, 100, and 100% for 10 min each step) and then in propylene oxide (PO) (100 and 100%, 30 min each step). Infiltration was performed using LX112 epoxy resin with BDMA (21212, Ladd) in serial PO dilutions steps, each lasting 4 hours (25% resin/75% PO, 50% resin/50% PO, 75% resin/25% PO, 100% resin, and 100% resin). Samples were mounted in fresh resin in hollowed mouse cortex slabs, which provide a tissue consistency similar to that of the zebrafish brain. This approach, inspired by Hildebrand *et al.* (*75*), prevents the sample from sinking to the bottom of the resin mold and significantly improves sectioning reliability. Mouse tissue was fixed using standard procedures (*77*) and then cut into 2- to 3-mm wide cubes that were pierced using a puncher (0.75 mm; 57395, Electron Microscopy Sciences) to insert the larva. The cubes were stained along with fish samples using the protocol described above except that the uranyl acetate overnight step was performed at RT. The samples were then cured with support tissue during 3 days at 60°C. For all steps, a rotator was used. Aqueous solutions were prepared with water passed through a purification system (Arium 611VF, Sartorius Stedim Biotech). The protocol lasted 5 consecutive days including surgery, fixation, staining, and resin embedding followed by 3 days of resin curing.

EM image alignment, stitching, rendering, and neuronal morphology proofreading

We trained convolutional neural networks to segment cells, detect synaptic clefts, compute their sizes, and assign presynaptic and postsynaptic objects from the cell segmentation at each cleft (*78*). Cell segmentation and synapse detection and assignment used the aligned image with locations in the "image mask" set to black. All synapses in this study were manually inspected. Last, cell segmentation was ingested into the ChunkedGraph proofreading system so that morphological errors could be manually corrected, and synapses were ingested into an annotation table for consistent analysis (*79*).

Cell-type determination, multimodal, and brain regions registrations

To determine whether neurons were inhibitory, we manually traced a mask surrounding the neurons' nuclei in the green channel and computed the average corresponding red fluorescence. Neurons with values superior to 10% of the maximum red signal (25 on an 8-bit scale) were considered inhibitory, while the others were considered excitatory. In the OT, nearly all neurons express either Gad1b or Vglut2a with minimal overlap (*45*, *80*), supporting this distinction.

Matching of neuronal identities from the two-photon imaging to the EM volume was performed by manual registration using the Fiji plugin BigWarp (*81*). The two-photon image stack (*z*-steps of 2 μm, containing green and red fluorescence) signal-to-noise ratio was first enhanced using content-aware image restoration (*82*) and then registered to a downsampled EM stack (0.512 by 0.512 by 0.480 μm/pixel) using 771 landmarks. This EM stack was downloaded from Neuroglancer (https://github.com/google/neuroglancer) using CloudVolume (*83*). The quality of the mapping was exhaustively assessed visually, and fluorescently labeled blood vessels, which were not used as landmarks for the registration, allowed us to independently confirm the quality of the mapping. Figure S5A illustrates the registration quality in the OT. Deformed planes of green and red fluorescence (8-bit image stacks) were uploaded to Neuroglancer using CloudVolume, enabling collaborative reconstruction and cell-type determination of the neurons of interest.

ITNs were identified by manually registering a *Tg*(*HuC:H2B-GCaMP6s;* ^{ITN}*Gal4*, *UAS:RFP*) whole-brain two-photon stack acquired at 7 dpf to a downsampled EM stack (0.512 μm by 0.512 μm by 0.480 μm/pixel) using 73 landmarks using BigWarp (*81*). The registered stack of green and red fluorescence was uploaded to Neuroglancer as described above. Proofreading of the ITNs axons confirmed that

they crossed to the contralateral hemisphere, consistent with previous descriptions (*41*). As our two-photon imaging did not include this ventral region, we assumed, following the same study, that all ITNs are inhibitory.

To confirm that PVPNs project to the hindbrain, we registered the EM stack to the Z-Brain reference atlas (*84*), which includes annotated brain regions. We manually selected 207 landmarks between the EM stack and the *Tg*(*elavl3:H2B-RFP*) confocal stack in the Z-Brain coordinate system to generate a bridge transform using BigWarp (*81*). Reticulospinal neurons were identified using Orger *et al.* (*85*).

Calcium imaging to characterize RGCs functional activity

To monitor calcium dynamics, we used a commercial 2P scanning microscope (LAVision, Miltenyi Biotec) coupled with a tunable Ti:Sapphire femtosecond laser (Coherent Chameleon, wavelength range of 700 to 1100 nm). Calcium transients were acquired via bidirectional galvo-galvo scanning at 920 nm, with a scanning rate of 3 Hz and a field of view of 300 μm by 300 μm.

Visual stimulation for calcium imaging

Visual stimuli were delivered using a red-emitting projector (spectrum shown in fig. S10), projecting on a diffusive screen positioned at ~3 cm from the larva's head and covering 120° horizontal visual field. The visual stimuli sequence consisted in: (i) bright flash: a single 10-s bright flash stimulus; (ii) gratings: four gratings corresponding to the cardinal directions (0°, 90°, 180°, and 270°) with 10°-wide dark stripes moving at 20°/s. Each grating was presented statically in the first set of stimuli and then in motion for 5 s in the second set of stimuli; (iii) bright ramp: a gradual increase in brightness over 5 s; (iv) looming stimuli: a steady looming, a dark circular dot whose dimension expands at a constant rate of 20°/s, followed by an exponential looming, with lateral dimensions doubling every second; (v) dark ramp: a gradual decrease in brightness over 5 s. A second sequence consisted in: (i) prey-dot stimuli: a 5-μm dot moving horizontally four times back and forth at a speed of 80°/s with the stimulus repeated twice. (ii) Gratings: same as in the first sequence. Stimuli were programmed and synchronized with calcium imaging recordings, ensuring precise timing and reproducibility.

Analysis of visually induced calcium responses

Single-ROI traces were extracted using the Suite2p software, applying its functional detection module following motion correction. ROI detection was performed with a threshold scaling factor of 0.75 and a maximum allowed ROI overlap of 1. Raw fluorescence traces (F) were extracted for each ROI, and neuropil correction was applied using the default coefficient (0.7 × Fneu). ROIs located within the same neuropil layer, manually identified on the basis of anatomy and their distance from the skin, were normalized to their respective baseline values (mode of the raw fluorescence trace) before averaging across ROIs to yield a single calcium trace per layer, per fish. Calcium transients were defined as $\Delta F/F = [F(t) - F_0]/F_0$, with F_0 being the mode of the trace. The resulting average calcium transients per layer were further normalized to their respective maximum values. Last, normalized traces from individual fish were averaged to obtain a single representative calcium transient for each layer. These normalized traces were subsequently analyzed using a customized approach based on the OASIS package implemented in a MATLAB environment (*86*). A first full trace deconvolution was performed based on a second-order autoregressive kernel, constructed as the difference between a rising and a decaying exponential. The resulting neuronal activity trace (a set of discrete peaks representing the individual events that generate the overall calcium transients) was then decomposed into multiple time windows, corresponding to the duration of the different visual stimuli presented to the larva. Subsequently, activity peaks corresponding to the stimuli of interest were reconvolved with the kernel function to evaluate the contribution of each stimulus to the global calcium responses and to separate it from interstimulus cross-talk, as well as from the effects of transitions between stimulation patterns and from spontaneous activity. The peak values of the calcium responses corresponding to each stimulus were then used to quantitatively compare the magnitude of the responses across layers and visual stimuli.

Quantification and statistical analyses

Custom codes used for image analyses and quantifications are available at https://github.com/del-bene-lab/lrrn_zebrafish/tree/main. All comparisons between WT controls and mutant larvae were carried out on Prism 7 (GraphPad software). To assess statistical significance the Mann-Whitney test by ranks was performed when the dataset did not follow a normal distribution or did not meet basic *t* test assumptions. When applicable, randomized analyses, blinding, and exclusion criteria based on independent technical issues were proceeded. Figures were prepared using Prism 7 (GraphPad software) and MATLAB R2023a, with data exported to Adobe 2024 Photoshop 25.5.1 and Illustrator 28.4.1 for final formatting.

Use of AI-assisted tools

ChatGPT (OpenAI, GPT-4) and Grammarly (Grammarly Inc., 2025 version) were used exclusively for language editing, using the following prompt: "Improve the language of the text." No scientific content, data analysis, or interpretation was generated by these tools. All outputs were reviewed and verified by the authors, who take full responsibility for the content.

Supplementary Materials

The PDF file includes:

Figs. S1 to S10
Legends for movies S1 and S2
Tables S1 to S3

Other Supplementary Material for this manuscript includes the following:

Movies S1 and S2

REFERENCES

1. J. B. Girault, The developing visual system: A building block on the path to autism. *Dev. Cogn. Neurosci.* **73**, 101547 (2025).
2. M. D. Ketkar, K. Sporar, B. Gür, G. Ramos-Traslosheros, M. Seifert, M. Silies, Luminance information is required for the accurate estimation of contrast in rapidly changing visual contexts. *Curr. Biol.* **30**, 657–669.e4 (2020).
3. B. Khan, O. Mongkol Jaesiri, I. P. Lazarte, Y. Li, G. Tian, P. Zhao, Y. Zhao, V. D. Ho, J. L. Semmelhack, Zebrafish larvae use stimulus intensity and contrast to estimate distance to prey. *Curr. Biol.* **33**, 3179–3191.e4 (2023).
4. J. A. Sahel, E. Boulanger-Scemama, C. Pagot, A. Arleo, F. Galluppi, J. N. Martel, S. D. Esposti, A. Delaux, J. B. de Saint Aubert, C. de Montleau, E. Gutman, I. Audo, J. Duebel, S. Picaud, D. Dalkara, L. Blouin, M. Taiel, B. Roska, Partial recovery of visual function in a blind patient after optogenetic therapy. *Nat. Med.* **27**, 1223–1229 (2021).
5. M. Shinza-Kameda, E. Takasu, K. Sakurai, S. Hayashi, A. Nose, Regulation of layer-specific targeting by reciprocal expression of a cell adhesion molecule, Capricious. *Neuron* **49**, 205–213 (2006).
6. T. C. Badea, H. Cahill, J. Ecker, S. Hattar, J. Nathans, Distinct roles of transcription factors Brn3a and Brn3b in controlling the development, morphology, and function of retinal ganglion cells. *Neuron* **61**, 852–864 (2009).

7. R. J. Vigouroux, K. Duroure, J. Vougny, S. Albadri, P. Kozulin, E. Herrera, K. Nguyen-Ba-Charvet, I. Braasch, R. Suárez, F. Del Bene, A. Chédotal, Bilateral visual projections exist in non-teleost bony fish and predate the emergence of tetrapods. *Science* **372**, 150–156 (2021).
8. K. S. Pappu, M. Morey, A. Nern, B. Spitzweck, B. J. Dickson, S. L. Zipursky, Robo-3-mediated repulsive interactions guide R8 axons during *Drosophila* visual system development. *Proc. Natl. Acad. Sci. U.S.A.* **108**, 7571–7576 (2011).
9. N. Nikolaou, M. P. Meyer, Lamination speeds the functional development of visual circuits. *Neuron* **88**, 999–1013 (2015).
10. K. S. Cramer, I. J. Miko, Eph-ephrin signaling in nervous system development. *F1000Research* **5**, 1–9 (2016).
11. A. E. West, M. E. Greenberg, Neuronal activity-regulated gene transcription in synapse development and cognitive function. *Cold Spring Harb. Perspect. Biol.* **3**, 1–21 (2011).
12. J. R. Sanes, S. L. Zipursky, Design principles of insect and vertebrate visual systems. *Neuron* **66**, 15–36 (2010).
13. J. S. Joly, G. Recher, A. Brombin, K. Ngo, V. Hartenstein, A conserved developmental mechanism builds complex visual systems in insects and vertebrates. *Curr. Biol.* **26**, R1001–R1009 (2016).
14. H. Baier, Synaptic laminae in the visual system: Molecular mechanisms forming layers of perception. *Annu. Rev. Cell Dev. Biol.* **29**, 385–416 (2013).
15. C. Lyu, Z. Li, C. Xu, K. K. L. Wong, D. J. Luginbuhl, C. N. McLaughlin, Q. Xie, T. Li, H. Li, L. Luo, Dimensionality reduction simplifies synaptic partner matching in an olfactory circuit. *Science* **388**, 538–544 (2025).
16. Y. Zhong, C. Desplan, Searching for partners. *Science* **388**, 468–469 (2025).
17. J. De Wit, W. Hong, L. Luo, A. Ghosh, Role of leucine-rich repeat proteins in the development and function of neural circuits. *Annu. Rev. Cell Dev. Biol.* **27**, 697–729 (2011).
18. J. R. Sanes, S. L. Zipursky, Synaptic specificity, recognition molecules, and assembly of neural circuits. *Cell* **181**, 536–556 (2020).
19. T. Moreland, F. E. Poulain, To stick or not to stick: The multiple roles of cell adhesion molecules in neural circuit assembly. *Front. Neurosci.* **16**, 889155 (2022).
20. Y. Carrier, L. Q. Rio, N. Formicola, L. Orts, A. Borst, F. Pinto-teixeira, Biased cell adhesion organizes the *Drosophila* visual motion integration circuit. *Dev. Cell 9*, 762–779 (2025).
21. H. Baier, E. K. Scott, The visual systems of zebrafish. *Annu. Rev. Neurosci.* **47**, 255–276 (2024).
22. J. S. Wolffsohn, K. L. Gifford, Optical strategy utilising contrast modulation to slow myopia. *Ophthalmol. Sci.* **5**, 100672 (2025).
23. H. Rahimi-Nasrabadi, J. Jin, R. Mazade, C. Pons, S. Najafian, J. M. Alonso, Image luminance changes contrast sensitivity in visual cortex. *Cell Rep.* **34**, 108692 (2021).
24. E. Robles, E. Laurell, H. Baier, The retinal projectome reveals brain-area-specific visual representations generated by ganglion cell diversity. *Curr. Biol.* **24**, 2085–2096 (2014).
25. T. Xiao, H. Baier, Lamina-specific axonal projections in the zebrafish tectum require the type IV collagen Dragnet. *Nat Neurosci.* **10**, 1529–1537 (2007).
26. D. Förster, T. O. Helmbrecht, D. S. Mearns, L. Jordan, N. Mokayes, H. Baier, Retinotectal circuitry of larval zebrafish is adapted to detection and pursuit of prey. *eLife* **9**, e58596 (2020).
27. Y. Kölsch, J. Hahn, A. Sappington, M. Stemmer, A. M. Fernandes, T. O. Helmbrecht, S. Lele, S. Butrus, E. Laurell, I. Arnold-Ammer, K. Shekhar, J. R. Sanes, H. Baier, Molecular classification of zebrafish retinal ganglion cells links genes to cell types to behavior. *Neuron* **109**, 645–662.e9 (2021).
28. C. Mencarelli, F. Pichaud, *Orthodenticle* is required for the expression of principal recognition molecules that control axon targeting in the *Drosophila* retina. *PLOS Genet.* **11**, e1005303 (2015).
29. L. C. Andreae, A. Lumsden, J. D. Gilthorpe, Chick Lrrn2, a novel downstream effector of Hoxb1 and Shh, functions in the selective targeting of rhombomere 4 motor neurons. *Neural Dev.* **4**, 27 (2009).
30. J. de Wit, E. Sylwestrak, M. L. O'Sullivan, S. Otto, K. Tiglio, J. N. Savas, J. R. Yates, D. Comoletti, P. Taylor, A. Ghosh, LRRTM2 interacts with neurexin1 and regulates excitatory synapse formation. *Neuron* **64**, 799–806 (2009).
31. S. Kim, A. Burette, H. S. Chung, S. K. Kwon, J. Woo, H. W. Lee, K. Kim, H. Kim, R. J. Weinberg, E. Kim, NGL family PSD-95-interacting adhesion molecules regulate excitatory synapse formation. *Nat. Neurosci.* **9**, 1294–1301 (2006).
32. S. B. Thyme, L. M. Pieper, E. H. Li, S. Pandey, Y. Wang, N. S. Morris, C. Sha, J. W. Choi, K. J. Herrera, E. R. Soucy, S. Zimmerman, O. Randlett, J. Greenwood, S. A. McCarroll, A. F. Schier, Phenotypic landscape of schizophrenia-associated genes defines candidates and their shared functions. *Cell* **177**, 478–491.e20 (2019).
33. B. Karimi, P. Silwal, S. Booth, N. Padmanabhan, S. H. Dhume, D. Zhang, N. Zahra, M. F. Jackson, G. J. Kirouac, J. H. Ko, J. W. Chopek, T. J. Siddiqui, Schizophrenia-associated LRRTM1 regulates cognitive behavior through controlling synaptic function in the mediodorsal thalamus. *Mol. Psychiatry* **26**, 6912–6925 (2021).
34. I. Sousa, T. Clark, R. Holt, A. Pagnamenta, E. Mulder, R. Minderaa, A. Bailey, A. Battaglia, S. Klauck, F. Poustka, A. Monaco, Polymorphisms in leucine-rich repeat genes are associated with autism spectrum disorder susceptibility in populations of European ancestry. *Mol. Autism* **1**, 7 (2010).
35. J. D. Burrill, S. S. Easter, Development of the retinofugal projections in the embryonic and larval zebrafish (*Brachydanio rerio*). *J. Comp. Neurol.* **346**, 583–600 (1994).
36. P. Dufourcq, S. Rastegar, U. Strähle, P. Blader, Parapineal specific expression of gfi1 in the zebrafish epithalamus. *Gene Expr. Patterns* **4**, 53–57 (2004).
37. C. Stringer, T. Wang, M. Michaelos, M. Pachitariu, Cellpose: A generalist algorithm for cellular segmentation. *Nat. Methods* **18**, 100–106 (2021).
38. M. P. Meyer, S. J. Smith, Evidence from in vivo imaging that synaptogenesis guides the growth and branching of axonal arbors by two distinct mechanisms. *J. Neurosci.* **26**, 3604–3614 (2006).
39. B. Xu, X. Tang, M. Jin, H. Zhang, L. Du, S. Yu, J. He, Unifying developmental programs for embryonic and postembryonic neurogenesis in the zebrafish retina. *Development* **147**, dev185660 (2020).
40. L. M. Nevin, E. Robles, H. Baier, E. K. Scott, The basic "macro-circuit" of the vertebrate visual system. *BMC Biol.* **8**, 126 (2010).
41. C. Gebhardt, T. O. Auer, P. M. Henriques, G. Rajan, K. Duroure, I. H. Bianco, F. Del Bene, An interhemispheric neural circuit allowing binocular integration in the optic tectum. *Nat. Commun.* **10**, 5471 (2019).
42. E. D. Spikol, J. Cheng, M. Macurak, A. Subedi, M. E. Halpern, Genetically defined nucleus incertus neurons differ in connectivity and function. *eLife* **12**, RP89516 (2023).
43. M. Folgueira, S. Riva-Mendoza, N. Ferreño-Galmán, A. Castro, I. H. Bianco, R. Anadón, J. Yáñez, Anatomy and connectivity of the torus longitudinalis of the adult zebrafish. *Front. Neural Circuits* **14**, 8 (2020).
44. P. M. Henriques, N. Rahman, S. E. Jackson, I. H. Bianco, Nucleus isthmi is required to sustain target pursuit during visually guided prey-catching. *Curr. Biol.* **29**, 1771–1786.e5 (2019).
45. J. Boulanger-Weill, R. L. Schalek, M. Petkova, S. Kumar, J. H. Savaliya, Y. Wu, G. F. P. Schuhknecht, H. Naumann, M. Eberle, K. N. Kirchberger, S. Rencken, I. H. Bianco, D. Baum, F. Del Bene, J. W. Lichtman, A. Bahl, Correlative light and electron microscopy reveals the fine circuit structure underlying evidence accumulation in larval zebrafish. bioRxiv 643363 [Preprint] (2025). https://doi.org/10.1101/2025.03.14.643363.
46. V. Di Donato, F. De Santis, S. Albadri, T. O. Auer, K. Duroure, M. Charpentier, J. P. Concordet, C. Gebhardt, F. Del Bene, An attractive reelin gradient establishes synaptic lamination in the vertebrate visual system. *Neuron* **97**, 1049–1062.e6 (2018).
47. I. Temizer, J. C. Donovan, H. Baier, J. L. Semmelhack, A visual pathway for looming-evoked escape in larval zebrafish. *Curr. Biol.* **25**, 1823–1834 (2015).
48. I. H. Bianco, F. Engert, Visuomotor transformations underlying hunting behavior in zebrafish. *Curr. Biol.* **25**, 831–846 (2015).
49. S. I. Zhu, G. J. Goodhill, From perception to behavior: The neural circuits underlying prey hunting in larval zebrafish. *Front. Neural Circuits* **17**, 1087993 (2023).
50. Q. Lo Giudice, M. Leleu, G. La Manno, P. J. Fabre, Single-cell transcriptional logic of cell-fate specification and axon guidance in early-born retinal neurons. *Development* **146**, dev178103 (2019).
51. M. Fernández-Nogales, M. T. López-Cascales, V. Murcia-Belmonte, A. Escalante, J. Fernández-Albert, R. Muñoz-Viana, A. Barco, E. Herrera, Multiomic analysis of neurons with divergent projection patterns identifies novel regulators of axon pathfinding. *Adv. Sci.* **9**, e2200615 (2022).
52. M. Milan, U. Weihe, L. Pérez, S. M. Cohen, The LRR proteins capricious and tartan mediate cell interactions during dv boundary formation in the *Drosophila* wing. *Cell* **106**, 785–794 (2001).
53. H. Kohsaka, A. Nose, Target recognition at the tips of postsynaptic filopodia: Accumulation and function of capricious. *Development* **136**, 1127–1135 (2009).
54. M. Kurusu, A. Cording, M. Taniguchi, K. Menon, E. Suzuki, K. Zinn, A screen of cell-surface molecules identifies leucine-rich repeat proteins as key mediators of synaptic target selection. *Neuron* **59**, 972–985 (2008).
55. A. Meier, R. Nelson, V. P. Connaughton, Color processing in zebrafish retina. *Front. Cell. Neurosci.* **12**, 327 (2018).
56. T. Yoshimatsu, C. Schröder, N. E. Nevala, P. Berens, T. Baden, Fovea-like photoreceptor specializations underlie single UV cone driven prey-capture behavior in zebrafish. *Neuron* **107**, 320–337.e6 (2020).
57. I. H. Bianco, A. R. Kampff, F. Engert, Prey capture behavior evoked by simple visual stimuli in larval zebrafish. *Front. Syst. Neurosci.* **5**, 101 (2011).
58. Y. Xiao, L. Petrucco, L. J. Hoodless, R. Portugues, T. Czopka, Oligodendrocyte precursor cells sculpt the visual system by regulating axonal remodeling. *Nat. Neurosci.* **25**, 280–284 (2022).
59. F. Kroll, G. T. Powell, M. Ghosh, G. Gestri, P. Antinucci, T. J. Hearn, H. Tunbak, S. Lim, H. W. Dennis, J. M. Fernandez, D. Whitmore, E. Dreosti, S. W. Wilson, E. J. Hoffman, J. Rihel, A simple and effective F0 knockout method for rapid screening of behaviour and other complex phenotypes. *eLife* **10**, e59683 (2021).
60. J. Bussmann, S. Schulte-Merker, Rapid BAC selection for tol2-mediated transgenesis in zebrafish. *Development* **138**, 4327–4332 (2011).
61. M. L. Suster, G. Abe, A. Schouw, K. Kawakami, Transposon-mediated BAC transgenesis in zebrafish. *Nat. Protoc.* **6**, 1998–2021 (2011).

62. D. Balciunas, K. J. Wangensteen, A. Wilber, J. Bell, A. Geurts, S. Sivasubbu, X. Wang, P. B. Hackett, D. A. Largaespada, R. S. McIvor, S. C. Ekker, Harnessing a high cargo-capacity transposon for genetic applications in vertebrates. *PLOS Genet.* **2**, 1715–1724 (2006).
63. A. J. Pittman, M.-Y. Law, C.-B. Chien, Pathfinding in a large vertebrate axon tract: Isotypic interactions guide retinotectal axons at multiple choice points. *Development* **135**, 2865–2871 (2008).
64. T. O. Auer, F. Del Bene, CRISPR/Cas9 and TALEN-mediated knock-in approaches in zebrafish. *Methods* **69**, 142–150 (2014).
65. K. M. Kwan, E. Fujimoto, C. Grabher, B. D. Mangum, M. E. Hardy, D. S. Campbell, J. M. Parant, H. J. Yost, J. P. Kanki, C. Chien, The Tol2kit: A multisite gateway-based construction kit for *Tol2* transposon transgenesis constructs. *Dev. Dyn.* **236**, 3088–3099 (2007).
66. J. Kaslin, V. Kroehne, F. Benato, F. Argenton, M. Brand, Development and specification of cerebellar stem and progenitor cells in zebrafish: from embryo to adult. *Neural. Dev.* **8**, 9 (2013).
67. T. O. Auer, T. Xiao, V. Bercier, C. Gebhardt, K. Duroure, J.-P. Concordet, C. Wyart, M. Suster, K. Kawakami, J. Wittbrodt, H. Baier, F. Del Bene, Deletion of a kinesin I motor unmasks a mechanism of homeostatic branching control by neurotrophin-3. *eLife* **4**, e05061 (2015).
68. N. J. Gosse, L. M. Nevin, H. Baier, Retinotopic order in the absence of axon competition Nathan. *Nature* **462**, 211–224 (2008).
69. C. Shi, J. Lu, W. Wu, F. Ma, J. Georges, H. Huang, J. Balducci, Y. Chang, Y. Huang, Endothelial cell-specific molecule 2 (ECSM2) localizes to cell-cell junctions and modulates bFGF-directed cell migration via the ERK-FAK pathway. *PLOS ONE* **6**, e21482 (2011).
70. G. Rajan, J. Lafaye, G. Faini, M. Carbo-Tano, K. Duroure, D. Tanese, T. Panier, R. Candelier, J. Henninger, R. Britz, B. Judkewitz, C. Gebhardt, V. Emiliani, G. Debregeas, C. Wyart, F. Del Bene, Evolutionary divergence of locomotion in two related vertebrate species. *Cell Rep.* **38**, 110585 (2022).
71. G. Rajan, G. Debregeas, M. B. Orger, F. Del Bene, An analysis pipeline to compare explorative locomotion across fish species. *STAR Protoc.* **3**, 101850 (2022).
72. V. Štih, L. Petrucco, A. M. Kist, R. Portugues, Stytra: An open-source, integrated system for stimulation, tracking and closed-loop behavioral experiments. *PLOS Comput. Biol.* **15**, e1006699 (2019).
73. L. A. Lister, C. P. Robertson, T. Lepage, S. L. Johnson, D. W. Raible, Nacre encodes a zebrafish microphthalmia-related protein that regulatesneural-crest-derived pigment cell fate. *Development* **126**, 3757–3767 (1999).
74. J. C. Tapia, N. Kasthuri, K. J. Hayworth, R. Schalek, J. W. Lichtman, S. J. Smith, J. Buchanan, High-contrast en bloc staining of neuronal tissue for field emission scanning electron microscopy. *Nat. Protoc.* **7**, 193–206 (2012).
75. D. G. C. Hildebrand, M. Cicconet, R. M. Torres, W. Choi, T. M. Quan, J. Moon, A. W. Wetzel, A. Scott Champion, B. J. Graham, O. Randlett, G. S. Plummer, R. Portugues, I. H. Bianco, S. Saalfeld, A. D. Baden, K. Lillaney, R. Burns, J. T. Vogelstein, A. F. Schier, W. C. A. Lee, W. K. Jeong, J. W. Lichtman, F. Engert, Whole-brain serial-section electron microscopy in larval zebrafish. *Nature* **545**, 345–349 (2017).
76. Y. Hua, P. Laserstein, M. Helmstaedter, Large-volume en-bloc staining for electron microscopy-based connectomics. *Nat. Commun.* **6**, 7923 (2015).
77. T. Fang, X. Lu, D. Berger, C. Gmeiner, J. Cho, R. Schalek, H. Ploegh, J. Lichtman, Nanobody immunostaining for correlated light and electron microscopy with preservation of ultrastructure. *Nat. Methods* **15**, 1029–1032 (2018).
78. T. Macrina, K. Lee, R. Lu, N. L. Turner, J. Wu, S. Popovych, W. W. Silversmith, N. Kemnitz, J. A. Bae, M. A. Castro, S. Dorkenwald, A. Halageri, Z. Jia, C. Jordan, K. Li, E. Mitchell, S. S. Mondal, S. Mu, B. Nehoran, W. Wong, S. Yu, A. L. Bodor, D. Brittain, J. Buchanan, D. J. Bumbarger, E. Cobos, F. Collman, L. Elabbady, P. G. Fahey, E. Froudarakis, D. Kapner, S. Kinn, G. Mahalingam, S. Papadopoulos, S. Patel, C. M. Schneider-Mizell, F. H. Sinz, M. Takeno, R. Torres, W. Yin, X. Pitkow, J. Reimer, A. S. Tolias, R. C. Reid, N. M. da Costa, H. S. Seung, Petascale neural circuit reconstruction: Automated methods. bioRxiv 455162 [Preprint] (2021). https://doi.org/10.1101/2021.08.04.455162.
79. S. Dorkenwald, C. M. Schneider-Mizell, D. Brittain, A. Halageri, C. Jordan, N. Kemnitz, M. A. Castro, W. Silversmith, J. Maitin-Shephard, J. Troidl, H. Pfister, V. Gillet, D. Xenes, J. A. Bae, A. L. Bodor, J. Buchanan, D. J. Bumbarger, L. Elabbady, Z. Jia, D. Kapner, S. Kinn, K. Lee, K. Li, R. Lu, T. Macrina, G. Mahalingam, E. Mitchell, S. S. Mondal, S. Mu, B. Nehoran, S. Popovych, M. Takeno, R. Torres, N. L. Turner, W. Wong, J. Wu, W. Yin, S. Yu, R. C. Reid, N. M. da Costa, H. S. Seung, F. Collman, CAVE: Connectome annotation versioning engine. bioRxiv 550598 [Preprint] (2023). https://doi.org/10.1101/2023.07.26.550598.
80. S. Higashijima, G. Mandel, J. R. Fetcho, Distribution of prospective glutamatergic, glycinergic, and GABAergic neurons in embryonic and larval zebrafish. *J. Comp. Neurol.* **480**, 1–18 (2004).
81. J. A. Bogovic, P. Hanslovsky, A. Wong, S. Saalfeld, Robust registration of calcium images by learned contrast synthesis. arXiv:1511.01154 (2016).
82. M. Weigert, U. Schmidt, T. Boothe, A. Müller, A. Dibrov, A. Jain, B. Wilhelm, D. Schmidt, C. Broaddus, S. Culley, M. Rocha-Martins, F. Segovia-Miranda, C. Norden, R. Henriques, M. Zerial, M. Solimena, J. Rink, P. Tomancak, L. Royer, F. Jug, E. W. Myers, Content-aware image restoration: Pushing the limits of fluorescence microscopy. *Nat. Methods* **15**, 1090–1097 (2018).
83. W. Silversmith, A. Zlateski, J. A. Bae, I. Tartavull, N. Kemnitz, J. Wu, H. S. Seung, Igneous: Distributed dense 3D segmentation meshing, neuron skeletonization, and hierarchical downsampling. *Front. Neural Circuits* **16**, 977700 (2022).
84. O. Randlett, C. L. Wee, E. A. Naumann, O. Nnaemeka, D. Schoppik, J. E. Fitzgerald, R. Portugues, A. M. B. Lacoste, C. Riegler, F. Engert, A. F. Schier, Whole-brain activity mapping onto a zebrafish brain atlas. *Nat. Methods* **12**, 1039–1046 (2015).
85. M. B. Orger, A. R. Kampff, K. E. Severi, J. H. Bollmann, F. Engert, Control of visually guided behavior by distinct populations of spinal projection neurons. *Nat. Neurosci.* **11**, 327–333 (2008).
86. J. Friedrich, Z. Pengcheng, L. Paninski, Fast online deconvolution of calcium imaging data. *PLOS Comput. Biol.* **13**, e1005423 (2017).

Acknowledgments: We thank all members of the Del Bene lab for discussions and the Institut de la Vision and Institute Curie animal and imaging facilities. We thank C. Fassier (Institut de la Vision) for discussions and for gifting us the *pCX* plasmids and S. Fouquet (Institut de la Vision) for constant help and advice in confocal imaging and IMARIS software. We thank N. Testa for the help in the initial screening of *gfi1ab*. AI-assisted technology (ChatGPT and Grammarly) was used to improve language during the writing process. **Funding:** This work was supported by the IHU FOReSIGHT (ANR-18-IAHU- 0001) (S.A. and F.D.B.); CNRS, INSERM, and Sorbonne Université core funding (F.D.B.); Zenith PhD Program (European Union's Horizon 2020 research and innovation program under the Marie Skłodowska-Curie actions, grant agreement no. 813457) (E.P. and F.D.B.); La Ligue Contre Le Cancer (fourth year PhD funding) (E.P.); European Research Council (ERC-2022-SYG grant 101071583 "TUBULINCODE") (F.D.B.); Fondation Berthe Fouassier (Fondation de France, nos. 201500060246 and 201600069985; S.A.); ANR JCJC (ANR-24-CE16-4532-01) FunCoRelax and IHU (P-FUNVIZ-IHU-000) (G.F.); NIH Grant U19NS104653 (F.En.); European Union's Horizon 2020 research and innovation programme under the Marie Skłodowska Curie grant agreement no. 945380 (G.O.-Á.); "la Caixa" Foundation (ID 100010434) "LCF/BQ/PR23/11980036 (G.O.-Á.); and AEI grants (PGC2018-095663-B-I00, PID2021-123261NB-I00, and CEX2018 000792M) and FEDER (C.P.).
Author contributions: Conceptualization: J.W.L. (EM dataset), E.P., F.D.B., and S.A. Investigation: E.P., G.F., J.T.-M.D., F.Eg., K.D., J.B.-W., J.W.L., and S.A. Methodology: J.H.S., J.B.-W., A.B., and J.W.L. (EM dataset), E.P., J.T.-M.D., J.V., G.O.-Á., F.D.B., and S.A. Resources: J.W.L., J.B.-W., F.En., A.B. (EM dataset), E.P., G.F., C.P., K.D., G.O.-Á., and S.A. Visualization: E.P., G.F., J.B.-W., A.B., F.En., J.W.L., and S.A. Software: J.W.L., A.B., and J.B.-W. (EM dataset), and E.P. Data curation: J.W.L., J.H.S., J.B.-W. (EM dataset), E.P., and S.A. Formal analysis: E.P., G.F., J.B.-W., and S.A. Validation: J.T.-M.D., E.P., G.F., and S.A. Funding acquisition: E.P., G.F., A.B., F.En., J.W.L., F.D.B., and S.A. Supervision: J.W.L. (EM dataset), E.P., F.D.B., and S.A. Writing—original draft: E.P., K.D., F.D.B., and S.A. Writing—review and editing: E.P., G.F., K.D., J.B.-W., J.H.S., F.D.B., and S.A. Project administration: F.En. (EM dataset), E.P., F.D.B., and S.A. **Competing interests:** The authors declare that they have no competing interests. **Data and materials availability:** All data needed to evaluate the conclusions in the paper including DNA/RNA sequences and custom codes are available for readers in the paper. Materials used for the analyses (transgenic lines and DNA constructs) are available upon request at shahad.albadri@inserm.fr or filippo.del-bene@inserm.fr.

Submitted 2 June 2025
Accepted 22 December 2025
Published 23 January 2026
10.1126/sciadv.adz4585

ScienceAdvances

Lrrn-mediated retinal ganglion cell targeting drives visual circuit assembly for brightness and contrast detection

Elena Putti, Giulia Faini, Julie Thanh-Mai Dang, Jay H. Savaliya, Fanny Eggeler, Karine Duroure, Juliette Vougny, Gonzalo Ortiz-Álvarez, Cristina Pujades, Armin Bahl, Jeff W. Lichtman, Florian Engert, Jonathan Boulanger-Weill, Filippo Del Bene, and Shahad Albadri

Sci. Adv. **12** (4), eadz4585. DOI: 10.1126/sciadv.adz4585